8-18-2011

Ros-Drill Automation: Visual Feedback Control And Rotational Motion Tracking

Jhon F. Diaz
Jhon F Diaz, jhon.diaz@engr.uconn.edu

Ros-Drill© Automation:

Visual Feedback Control and Rotational Motion Tracking

Jhon Fredy Diaz

B.S., Universidad Industrial de Santander, 2003

A Thesis

Submitted in Partial Fulfillment of the

Requirements for the Degree of

Master of Science

at the

University of Connecticut

2011

APPROVAL PAGE

Master of Science Thesis

Ros-Drill© Automation:

Visual Feedback Control and Rotational Motion Tracking

Presented by

Jhon Fredy Diaz, B.S.

Major Advisor_____
Prof. Nejat Olgac

Associate Advisor_____
Prof. Tai-Hsi Fan

Associate Advisor_____
Prof. Mehmet Toner, Harvard Univ.

Associate Advisor_____
Prof. Robert Gao

University of Connecticut

2011

ACKNOWLEDGEMENTS

I want to express my gratitude to my advisor, Professor Nejat Olgac. While pursuing my master degree I got the best possible guidance from him. He is a good example of how commitment, responsibility and brightness can get us beyond obstacles. I wish to extend my admiration not only for the academic support but also for his personal advises that have strengthened me.

I am also grateful to Professors Mehmet Toner, Tai-Hsi Fan and Robert Gao for kindly accepting to be part of my committee and for their constructive comments and valuable suggestions on my thesis work. In addition, I am indebted to Professors Mehmet Toner (Harvard Medical School Massachusetts General Hospital), Kent C. Lloyd (University of California at Davis), John D. Biggers (Harvard Medical School) for their willingness and encouragement throughout my research work. I must thank to Dr. Ming-Wen Li (U.C. Davis) and Gloria Lee (Harvard Medical School Massachusetts General Hospital) for their constructive criticism, readiness and excellent experimental work.

None of this would have been possible either if I hadn't counted on excellent people like my lab-mates: Rudy Cepeda, Zhenyu Zhang, Mark Bacon and Mehdi Karzar-Jeddi, we shared all the experiences in a daily basis; and also my wife and family who always encouraged me to make this achievement a reality. To finish, I want to dedicate this work to my grandparents.

This work is partly sponsored by NIH R24RR018934-01 and NSF CBET-0828733

TABLE OF CONTENTS

LIST OF FIGURES

LIST OF TABLES

1. INTRODUCTION

ICSI (Intra-cytoplasmic sperm injection) is a broadly utilized technique for artificial fertilization. This approach is successfully performed in human oocytes as well as others such as mice and bovine. The mice oocytes attract special interest in the pharmaceutical community, because they show similar physical behavior to human eggs, they are easier to culture, furthermore mouse oocytes are used during the early stage of development of therapeutic drugs for humans. Common components in performing ICSI are shown in Figure 1.1. The holding pipette of approximately 100 μm of outer diameter (on the left), immobilizes the oocyte with a slight suction. The injecting pipette (outer diameter of 8 μm) contains the sperm head to be injected. The piercing through the zona and the membrane needs to be achieved with a minimal damage to facilitate a rapid healing. The focal point of the present research is on this process.

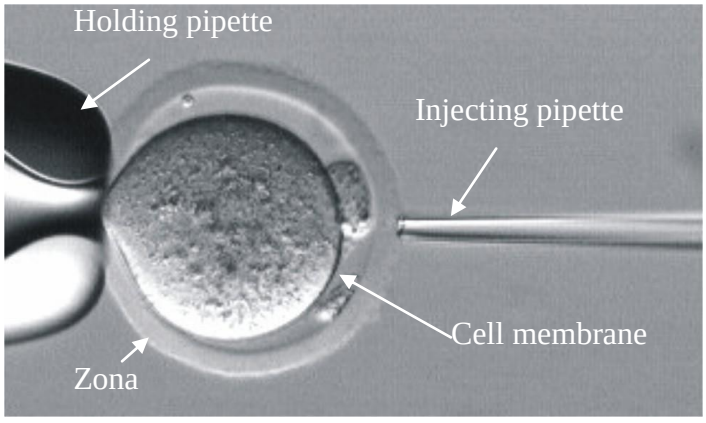

FIGURE 1.1: Experimental outlook of ICSI

The first application of ICSI, which is known as Conventional ICSI [1-3] is performed manually. With this technique, the tip of the injection pipette is advanced gently on the cytoplasmic membrane about halfway into the oocyte. Then it is pushed forward rapidly until it penetrates through the membrane. Conventional ICSI employs a spiked micropipette for facilitating penetration of the zona pellucida and piercing of the oolemma (cell membrane) [4-5]. Due to the high compliance of the mouse membrane, the penetration is very difficult without rupturing the ovum. Conventional ICSI has proven mostly unsuccessful (failure rate greater than 90% [1]) in most of the species including cattle, rat and mouse. The reason is attributed to the damage caused by the pressure of the injecting pipette on the cell membrane during the piercing process. If this damage does not heal properly, abnormal growth occurs in the future stages of development. To overcome this problem, an enhanced version of the process known as *Piezo-assisted ICSI*, has proved to increase the success rate beyond the conventional ICSI results [6-7]. In this technique, a piezo-activated axial force is applied to the injecting pipette to pierce smoothly the zona pellucida and then the cell membrane, causing minimal damage during the process. Piezo-assistance is, in fact, an important progress towards an automated deployment of micro-injection operation, with one caveat, however. The practitioners found it necessary to use a microscopically small mercury column in the tip of the piezo-assisted pipette in order to suppress its transverse oscillations which are harmful to the cell [8-10]. Due to high toxicity of mercury, this otherwise elegant technique could not garner a broad-base acceptance.

All ICSI fertilization techniques are expected to accomplish three goals: *i)* easily separate the sperm head from the tail, *ii)* enable the ICSI pipette to efficiently pierce and penetrate the zona pellucida and oolemma, and *iii)* facilitate injection of the sperm head without damage into the ovum. All three objectives have been demonstrated successfully in a recent study (Ergenc et al., [11]) using a novel, **rotationally oscillating drill (Ros-Drill©)** device. It does not require any mercury or a piezoelectric force actuator to drive a micropipette for performing ICSI in the mouse. Preliminary results of tests in mouse embryos showed that Ros-Drill-assisted ICSI gives survival, fertilization, embryo development, birth, and weaning rates comparable to those of piezo-assisted ICSI using mercury. Another important benefit of the new technology is related to its minimal demand on human expertise, and very short training periods for the operators (this happens to be one of the key motivations for the automation proposed in this work). These features result from the computer automated nature of the Ros-Drill© technology as explained by Ergenc and Olgac [12].

A schematic of the Ros-Drill© assembly is presented in Figure 1.2. The injecting pipette is connected to a small-precision motor which generates a high frequency but low amplitude oscillatory movement. In the next section a deeper explanation of Ros-Drill© performance is presented (the reader can also find the details of this α prototype in Ergenc et al., [11] and Ergenc and Olgac [12]).

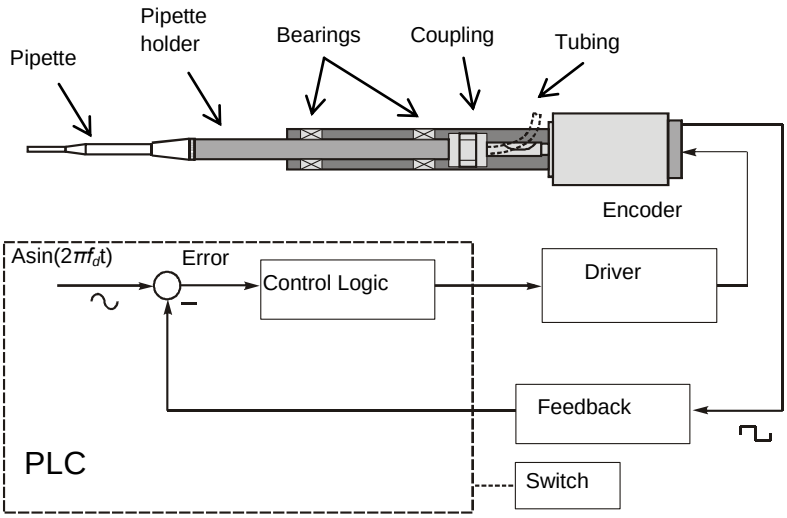

FIGURE 1.2: Ros-Drill© assembly and control system

DESCRIPTION OF ROS-DRILL© METHOD AND ITS AUTOMATION

A photograph of the α prototype is shown in Figure 1.3. A flexible coupling containing a channel accommodates the injection tubing. It is attached between the pipette holder and a micro-motor. The coupling transmits the angular motion from the motor to the pipette holder and also prevents axial misalignment. In Ros-Drill© operations, the pipette is smoothly forced into the oocyte as shown in Figure 1.4a-f first. Once a certain surface tension (and the corresponding radial deformation) of the membrane is reached, the rotational oscillation action is initiated. The objectives of the **automated Ross-Drill piercing** have two facets:

a) The automatic initiation of the pipette oscillations

b) High fidelity trajectory tracking of the oscillatory pipette motion,

.

A supervisory control is introduced for (a) using a visual feedback structure. A feedback control command for (b) to the DC motor is generated using a digital controller.

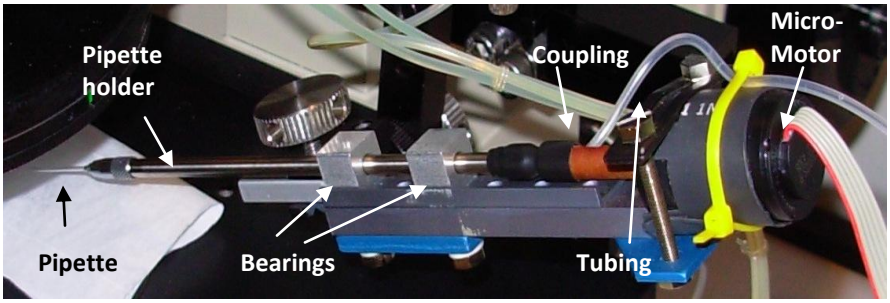

FIGURE 1.3: The α version Ros-Drill© prototype

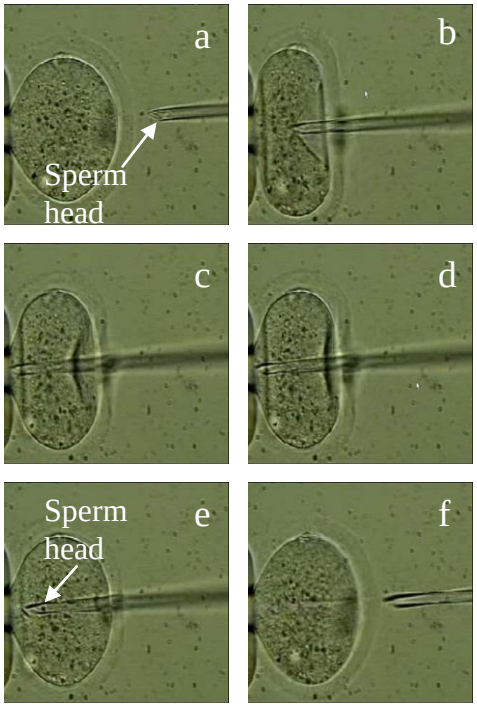

FIGURE 1.4: a-f. Deformation stages of the oocyte

The start of the drill action (item (a) above) is determined so far by the ICSI specialists in current practice. They guess the proper membrane deformation level, based on experience, in order to initiate the drilling. Obviously the real physical quantity, that is interpreted using this deformation information, is the surface tension on the membrane and it is not accessible for direct measurements. Once this predictive decision is made, the drilling (i.e., the rotational oscillations) starts. A part of the contributions in this research is in providing a scientific decision making framework to this initiation of Ros-Drill©.

The control structure ensures that the absolute angular position of the pipette returns to a designated zero configuration at the start of each rotation cycle in order to prevent the wrap-around of the connection tubing. In the rotational oscillations small angular amplitudes and high frequencies are selected due to two important reasons: first, to create relative motion between the membrane and the pipette tip (simply surpassing the membrane's bandwidth would do this), second, to prevent the lateral oscillations which may arise due to eccentricity of the pulled pipettes. The desired trajectory is simply defined as:

$$\theta_d = A_d \sin(2\pi f_d \cdot t) \tag{1}$$

where A_d corresponds to the desired amplitude (degrees) and f_d is the desired frequency (Hz). In the earlier works of Ros-Drill©, the amplitudes were lowered down to 0.2 degrees, and the operating frequencies were limited by 500 Hz. And the duration, T_d, was determined by the operator via a foot-switch. As such, the repeatability of T_d was always questionable. Figure 1.5 shows two examples of oscillatory profiles obtained by using the α prototype. It was proven in [11] that

this α version of Ros-Drill© could deliver similar results to piezo-assisted technique, which is the state-of-the-art method utilized in the ICSI labs.

The micropipette selection is also a critical issue for Ros-Drill©. During the first experiments with the α version Ros-Drill© straight (i.e., unbent) and beveled spike (30 degrees angled spike at the tip) pipettes were used with satisfactory performance. The recommended inner diameter is be 5mm (to accommodate the passage of the sperm head) and the outer diameter no larger than 7mm (to cause minimum damage).

Once automated, the practical utilization of the Ros-Drill© injector for ICSI is foreseen in two different tasks:

i) Sperm head separation from the tail (sperm preparation phase),

ii) Piercing of the oolemma and injection of the sperm head into the cytoplasm.

High rotational amplitudes and low frequencies are used for separating sperm heads from tails, and low rotational amplitudes and high frequencies are selected for piercing and penetrating oolemma. Primary coverage in this study is on the automation and improvements of the second mode (drilling)

The focus in this thesis is on the automation of initiation-duration and precise execution of the desired rotational pipette oscillations. To this end an elaborate visual feedback routine and a very focused micro-controller-based trajectory tracking mechanism are used as described in the following section.

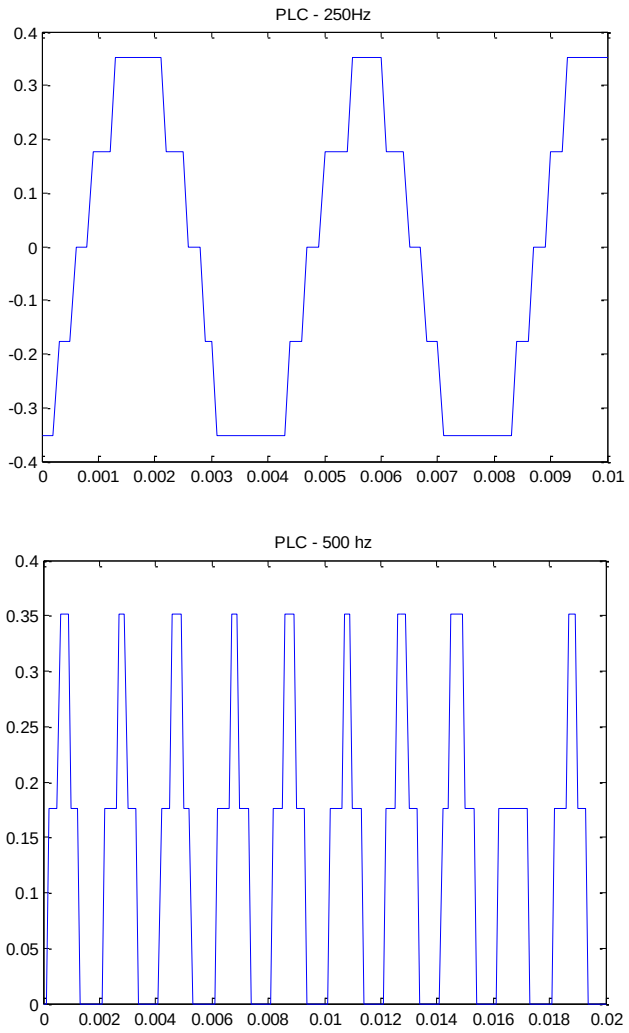

FIGURE 1.5: Oscillatory profiles for α version of Ros-Drill© with fixed amplitude. Upper: A_d = 0.36 degrees. Lower: A_d = 0.18 degrees. Notice the encoder resolution of 0.17 degree.

2. ROS-DRILL© AUTOMATION

Having a prototype that can produce good biological results in comparison with the currently utilized methods, we go two steps further in this study: Vision-based Ros-Drill© initiation automation and feedback control of rotational Ros-Drill© oscillations. Both are treated in this section.

2.1 VISION-BASED AUTOMATION FOR INITIATING THE OSCILLATIONS

Typical ICSI trials become a repetitive routine once the specialist gains the proper experience. Currently, the ICSI laboratories (medical and/or academic) perform a large number of these experiments per year. As shown in all ICSI documented research [1-3,11-12] the specialist decides when to start the force impulse that cause the cell membrane breaking, either piezo-assisted or Ros-drill-assisted ICSI. This makes injection process experience-dependent and very much empirical in nature, since the criterion to initiate the drilling motion depends strictly on the specialist expertise. In order to increase reliability and repeatability with Ros-Drill©, a technique is introduced in the present work, that allows an automatic evaluation of ICSI trials: Image processing of video frames delivered by a recording device connected to the microscope. In Figure 2.1 describes the general scheme that is followed to implement the mentioned automation. In effect, lack of a sensor to measure the membrane surface tension we rely on the visual characteristic of the oocyte to determine the initiation instant of the Ros-Drill© action. A digital CCD camera along with a TV acquisition card forms the frame-

grabbing system of ICSI trials. This information is sent to a computer to perform the image analysis and then based on the computational outcomes the signal to activate Ros-Drill© is generated and the oscillations started. Finding the proper feature that reveals the adequate geometric characteristic of the oocyte in the moment in which it is pierced, is the crux of the vision-based analysis. Two methods are proposed: oocyte curvature-based determination of the Ros-Drill© initiating point, and radial deformation-based determination scheme. Oocyte curvature analysis was developed with Prof. Tai-His Fan and a doctoral student Mehdi Karzar-Jeddi. The two methods offer a reliable outcome that prove to be adequate for piercing, however, they present considerable differences in required computation times, tipping the balance towards the radial deformation selection. Nevertheless we will explain both techniques in the text.

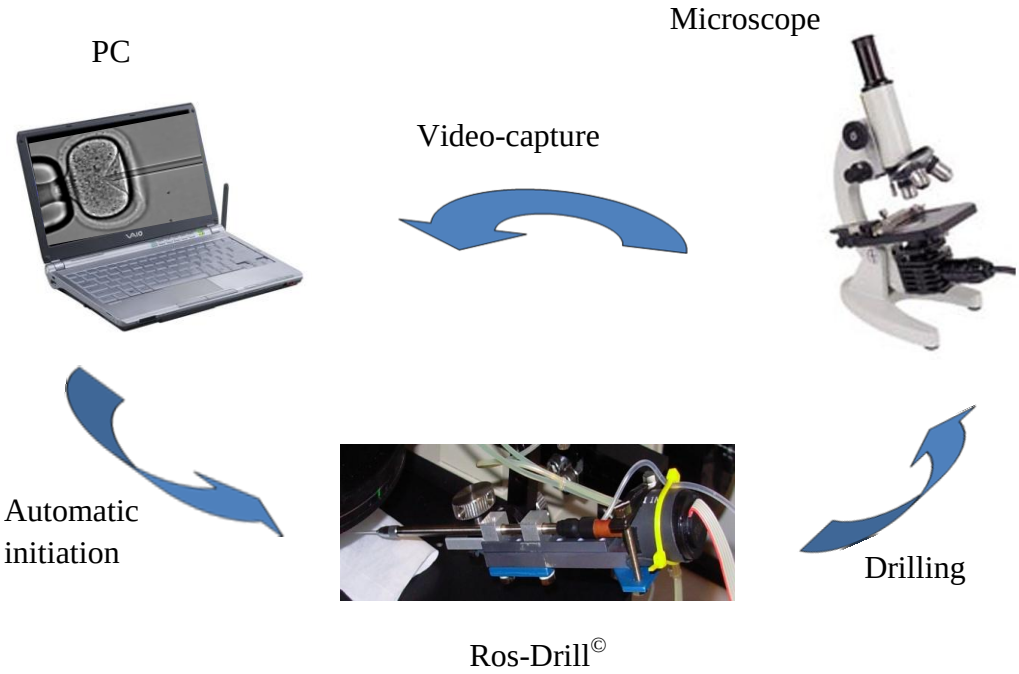

FIGURE 2.1: Scheme for Ros-Drill© automation

2.1.1 USING OOCYTE CURVATURES ANALYSIS

During an ICSI experiment, the oocyte changes dramatically its shape depending on the position of the injecting pipette along the axis of penetration. By evaluating the changes of the cell membrane (Figure 1.1), since the beginning when no deformation exists until the maximum healthy penetration appears, a tractable geometric feature is extracted. These experiments are regularly recorded as a set of still frames that altogether compound the sequence of the oocyte deformation. The first step consists of oocyte digital imaging in these still frames as proposed next.

- DIGITAL IMAGING OF THE OOCYTE

A set of images of Ros-Drill© operation is recorded through a CCD camera on the microscope. A sequence of frames is selected to observe the variations in some geometric properties of the oocyte as it is pierced. One of these properties is the radius of curvature. This knowledge can be used to determine when exactly the Ros-Drill© action should initiate. A computer-vision routine is performed first to monitor the membrane geometry. It uses MATLAB Image Processing Toolbox (MATLAB, 2010) over each frame to be analyzed.

Following is the specs of the vision equipment used: Inverted microscope OLYMPUS model IX70, 20X objective magnification. CCD Camera SONY XC-ST50/ST50CE with effective pixels 768x494, cell size 8.4 x 9.8 μm, chip size 7.96 x 6.45 mm. Video capture card: ATI TV WONDER, AVI, with maximum resolution for video-recording of 240x352, capture speed: 30 fps.

- IMAGE FILTERING

This routine converts each frame into gray-scale format and then it is cropped to zoom on only the oocyte section of the picture. To enhance the contrast of the image and to detect the cell membrane profile, the following Gaussian filter (a mask) is applied to the image:

$$f(j,k) = \frac{1}{2\pi\sigma^2}\exp\left[-\frac{1}{2\sigma^2}\left(j^2+k^2\right)\right] \quad (2)$$

where j and k are the symmetric integer counters (i.e., negative and positive) of which zero value represents the center of the mask, and σ is the standard deviation of the Gaussian distribution. When convolving a gray level picture with this mask, each pixel value is combined with the weighted values of the neighborhood pixels. The center pixel receives the highest weighting value and the weighting factor decays quickly as the distance from the origin increases (Figure 2.2). The smoothness of the Gaussian curve is determined by the range of j and k. The smaller these ranges the faster the filtering process would be, but the operation would lose the contrast quality at the image boundaries. We select a Gaussian filter that has a range of $-1 < j, k < 1$ creating a 3x3 filter mask. The standard deviation is taken as $\sigma=0.32$ in order to obtain the best contrast for the existing vision set-up. The ensuing mask is given numerically and pictorially in Figure 2.2.

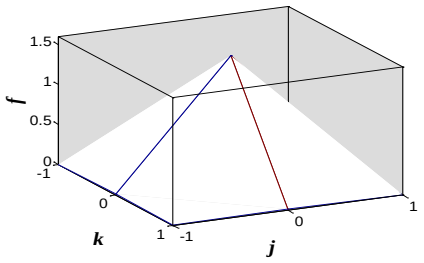

k \ j	-1	0	1
-1	0	0.012	0
0	0.012	1.554	0.012
1	0	0.012	0

FIGURE 2.2: Gaussian filter with a 3x3 mask array and standard deviation of 0.32

To improve the image contrast, the following **convolution** of the gray-scale image with the Gaussian mask is applied [13]:

$$N(j,k) = \sum_{k'=-1}^{1} \sum_{j'=-1}^{1} f(j',k') p(j-j',k-k') \tag{3}$$

where *p* corresponds to the gray-level pixel values of the image to be filtered, *f* is the filtering mask, and *N(j,k)* is the output image replacing all the *p(j,k)* gray levels. This convolution is illustrated in Figure 2.3 for a 3x3 mask.

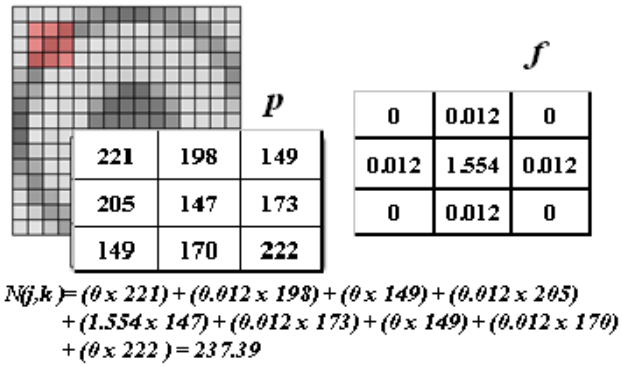

FIGURE 2.3: Display of Convolution Operation

The convolution operates over each pixel by taking a grid *p* (from the input image) of equal size to the mask *f* and then weighing the pixels as calculated

in Figure 2.3. For this example, the output pixel value “237.39” is stored in the position of the center pixel value (i.e., 147) in *p* for the output image after the filtering. The filtering effects to the frame are shown in Figure 2.4 below with a 3x3 mask. The filtered image (Figure 2.4b) shows the contrast clearly enhanced. The dark pixels are more differentiated from the bright ones.

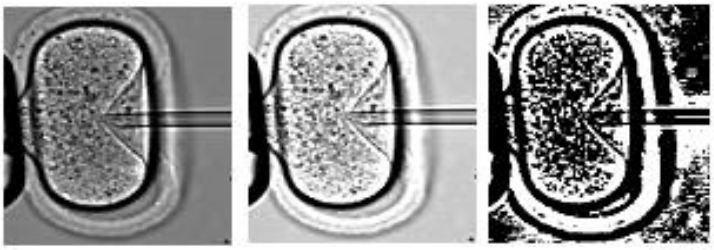

a. b. c.

FIGURE 2.4: Oocyte image before a. and after b. Gaussian filtering, c. Binarized filtered image

This filtered image with gray level from 0 to 255 is then further processed to a binary image, where black pixels come from values of 0 to 204 and white pixels from 205 to 255 (Figure 2.4c). This threshold value is selected to avoid the desired segmentation of the membrane profile when binarizing. The binary form is most effectively utilized next for tracing the boundaries of the membrane.

- TRACING THE CELL MEMBRANE PROFILE

A new routine was developed for this task. A starting point over the binary image is selected manually; this point must be on a segment of the membrane which is of interest. The black pixel nearest to this starting point is

then selected through a 3x3 pixel neighborhood grid, becoming the first point on the cell membrane profile. The next pixel on the cell membrane profile must be found through an evaluation of the neighbors of the center pixel *(i,j)* (the order of this evaluation is shown in zoomed inset on the left of Figure 2.5). This pixel must accomplish two conditions: its value must be "0" (black pixel) and it must be an additional pixel over the cell membrane profile. If the pixel # 1 (in Figure 2.5 blow-up on the left) does not accomplish both conditions the algorithm skips to the pixel # 2 and so on. When a new boundary pixel is found it will be the new center pixel *(i,j)* for the next iteration and the evaluation starts again for neighbor in position 1. By doing this, the location of points on the membrane is detected.

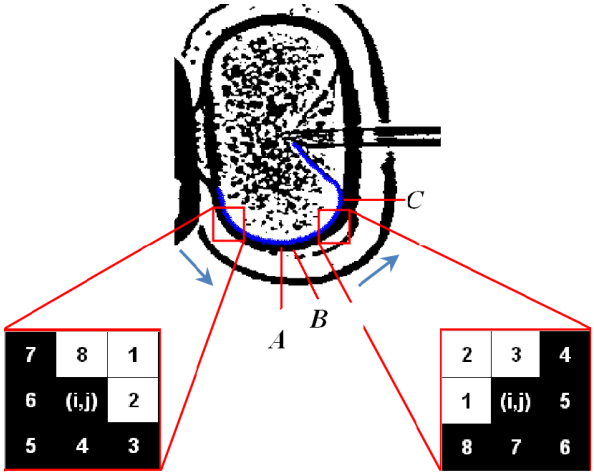

FIGURE 2.5: Cell membrane detection

When the membrane reaches a horizontal boundary, then pixel # 2 becomes black and this condition continues for several steps indicating that the trajectory will start rising (see point *A* on Figure 2.5). At this point the described membrane searching scheme should be performed in a different format in order to

avoid the acknowledgement of false boundary pixels. The new format changes the order of evaluation for neighbor pixels (as seen in the zoomed inset on the right of Figure 2.5), making the membrane evolves to an upward swing. Notice the symmetric features of the detection routine with respect to the vertical axis. If pixel # 4 is black the membrane climbs up at point *B*, and when pixel # 3 is black it will identify a transition of the grid at point *C*. Notice that these fundamental operations detect the **inner** edge of the membrane. This continues into the flat region of the membrane at the pipette location as shown and completes the necessary geometry.

As symmetry is assumed between the upper and lower halves of the oocyte membrane, only half oocyte is analyzed to give a general description of the cell deformation. The membrane points are defined and are stored in a matrix for further analysis. The curvature analysis follows this step of vision processing. This process is repeated for each frame at different stages of the cell deformation.

Just to give the reader an idea of the numerical load, the CPU time consumed for this image routine over a complete frame is approximately 0.89 sec using an Intel Core 6320 processor at 1.86 GHz with 2 Gbyte of RAM. This is deterministic for the geometric feature selection.

- CURVATURE DETERMINATION

The microinjection process has an axis-symmetric arrangement including the configuration of the holding and injection pipettes and a highly deformable

oocyte. Here it is proposed an algorithm to determine the real-time deformation of the cell membrane of the oocyte throughout the penetration process.

The curvature is important for predicting the local tension or compression force along the membrane surface, which is directly related to the required micropipette penetration force. The axis-symmetric membrane profile can be defined in the cylindrical coordinates, where *x* and *r* denote the axial and radial positions, respectively (Figure 2.6).

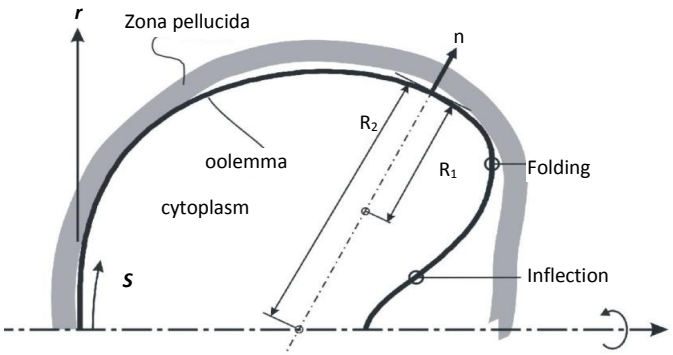

FIGURE 2.6: Cell Membrane Profile in the Cylindrical and Arc-length coordinate systems.

The coordinate origin is placed at the center of the holding pipette's mouth. A two-dimensional surface function is used to define the cell membrane profile in the meridian plane as

$$H(r,x) = r - f(x) = 0 \tag{4}$$

The corresponding outward surface normal ***n*** along the profile $H(r,x)$ is

$$n = \frac{\nabla H}{|\nabla H|} = \frac{-f'\hat{e}_x + \hat{e}_r}{\left(f'^2 + 1\right)^{1/2}} \tag{5}$$

The local surface curvature can then be derived from the divergence of the surface normal [14],

$$K(r,x) = \nabla \cdot n = K_1 + K_2 = \frac{-f''}{\left(f'^2 + 1\right)^{3/2}} + \frac{1}{f\left(f'^2 + 1\right)^{1/2}} \tag{6}$$

where K_1 and K_2, are the principal curvatures in the *r*-*x* plane and the conjugate plane, respectively. The inverse of the curvatures give the corresponding radii, $R_1 = 1/K_1$ and $R_2 = 1/K_2$. Because $f(x)$ is a multi-valued function, it is convenient to transform the curvature expression to a single-valued parametric form, $r=r(s)$, $x=x(s)$, and $K=K(s)$, where s is an arc-length coordinate starting from the mouth of the holding pipette. The arc-length coordinate follows the cell membrane profile till its intersection with the symmetry axis (Figure 2.6). The following generic curvature representation can then be derived using (4) and (6):

$$K(s) = \frac{r'^2 x' + x'^3 - r\,r''\,x' + r\,r'\,x''}{r\left(r'^2 + x'^2\right)^{3/2}} \tag{7}$$

$K(s)$ requires higher order derivatives of the parametric functions, $r(s)$ and $x(s)$, therefore the imaging data needs to be pre-processed to ensure that the representative membrane profile is sufficiently smooth for successive differentiation. The following smoothing algorithm are used in this study: *(i)* the coordinates of the raw data are redefined in terms of the arc-length coordinate using the standard cubic spline method [15], *(ii)* the Savitzky-Galoy filtering scheme [15] is applied to the new data points to increase the smoothness of the fit, *(iii)* the first- and second-order derivatives of $r(s)$ and $x(s)$ are calculated by the

cubic spline method or by a central difference scheme, *(iv)* the Savitzky-Galoy scheme is applied again to these derivatives before calculating the local curvature.

- DETERMINATION OF ROTATION INITIATION INSTANT

Researchers have attempted to automate the ICSI procedure as well as other similar tasks such as blastocyst microinjection with minimum human intervention [17-18]. Ideally automated system would execute most of the tasks that are performed by the human specialist. These tasks are: 1. holding the oocyte to pierce, 2. aspirating sperm head into injection pipette, 3. piercing zona pellucida and cell membrane of the oocyte and 4. injecting sperm head into the cytoplasm. All of them should be achieved using a non-invasive feedback mechanism, such as visual feedback [19] or force feedback [20]. In this work task (3), "piercing the cell membrane", is performed under visual feedback.

Figure 2.7 shows the comparison of the raw data with the smoothened and filtered membrane profiles.

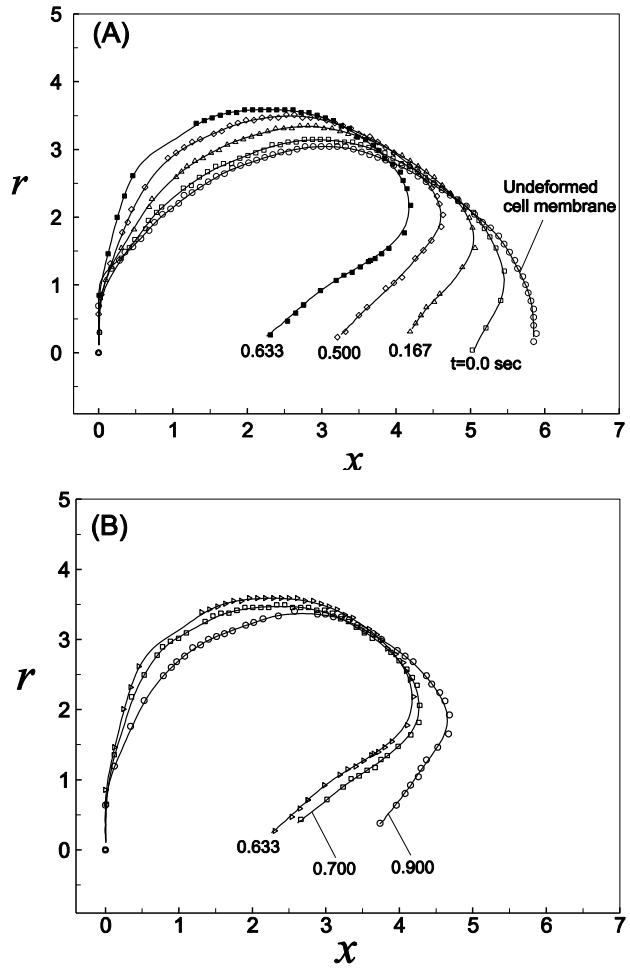

FIGURE 2.7: Transient membrane profiles in the meridian plane during the forward (a) and spring back (b) stages of penetration

Instantaneous images are taken including the undeformed membrane profile (for reference only) and the most deformed profile immediately before the penetration. The length scale is defined by the outer diameter of the injecting pipette (shown as *r* and *x* on Figure 2.7). The penetration process takes about 1 second. At time 0.633 second the cell membrane is pierced, and then it starts to spring back and resumes a relaxed state.

The CPU time on a desktop PC for analyzing each membrane profile, with 160 to 190 data points, is estimated to be 0.1 second including the input/output time. The goodness of the fit for the parametric functions *r(s)* and *x(s)* are examined by the square of the correlation coefficient R^2 [16], expressed as $R^2 = SSR/SST$ where

$$SSR = \sum_{i=1}^{n} \left(\hat{y}_i - \bar{y}\right)^2, \quad SST = \sum_{i=1}^{n} \left(y_i - \bar{y}\right)^2 \tag{8}$$

SST is the sum of the variability square for the dependent variable and *SSR* is the sum of the variability in the spline, y is the raw data from image processing, $\bar{y}$ is the average of the raw data and $\hat{y}$ is spline interpolation. The resulting correlation coefficients indicate that the fit to the raw edge data is highly correlated (R^2 around 0.98).

In Figure 2.8 the characteristics of the local curvatures and the radii of curvature are illustrated. It appears that the deformable cell membrane has two signature points: the **folding point** where *x* reaches the maximum value and $K_2 \rightarrow 0$, and the **inflection point** where $K_1 \rightarrow 0$ (Figure 2.6). At the folding point, the principal curvature K_2 changes to a negative value because the cell material is on the convex side of the membrane when it is observed from conjugate plane. Also near the folding point, the principal curvature K_1 remains positive till the inflection point since the cell material is on the concave side of the membrane in the meridian plane. In most of the dimensionless *s* domain from 0 up to approximately 0.8, both principal curvatures have similar order of magnitude, and

the value is close to 0.5, indicating that up to the folding point the membrane in this region has a sphere-like configuration. Passing through the folding point the sign of K_2 becomes negative.

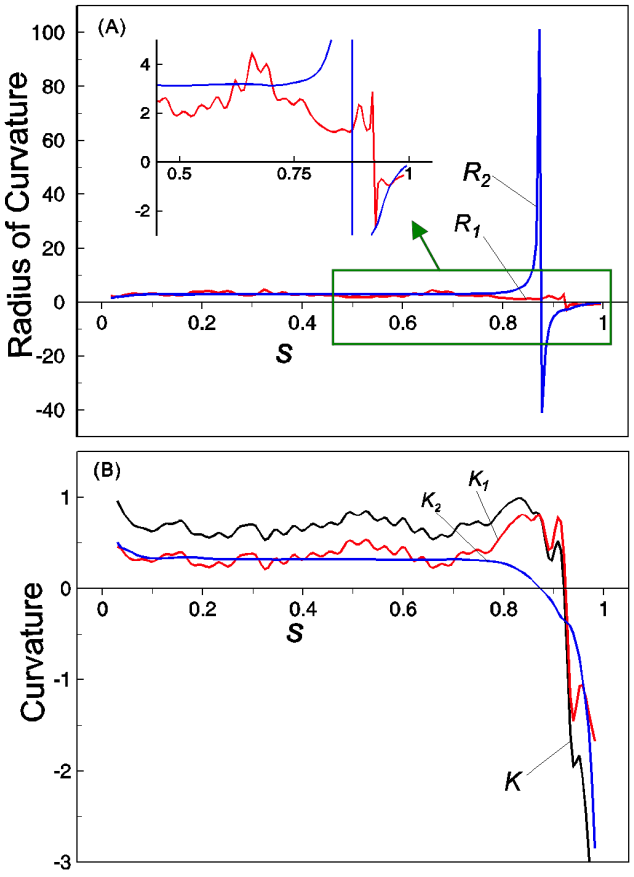

FIGURE 2.8: a. The radii of curvature on the *r-x* and the conjugate planes at $t = 0$. b. The corresponding curvatures *K1*, *K2* and *K*

After the inflection point, both principal curvatures become negative values. K_1 drops steeply at the inflection point due to the sign change. K_2 also decreases significantly in the narrowing region of the cone-shaped membrane. The membrane profile terminates at a cusp point where the curvature $K \rightarrow -\infty$. It is clear that the K_2 and R_2 curves are fairly smooth because only the first-order

derivative of the parametric form is involved in the calculation. However, the K_1 and R_1 curves entail second order derivatives, and thus they are relatively noisier (also the total curvature K). In Figure 2.8 the arc-length coordinate s is normalized by the total length of each profile after the filtering and smoothing process. The dimensionless curvature and radius of curvature are also scaled by the diameter and the inverse of the diameter of the injecting pipette, respectively.

Figure 2.9 shows the transient evolution of the curvatures corresponding to the membrane profiles in Figure 2.7. The folding point monotonically shifts inward (Figure 2.9b), whereas the inflection point tends to stay in a similar location (Figure 2.9a). The maximum principal curvature value K_1 increases during the penetration process, which is correlated to the shift of the folding point. The combined effect for the total curvature K gives a signature pattern which may suggest the proper onset point for automatic membrane piercing. Assuming that the fluid flow induced stress is negligible, the transient membrane evolution can be treated as a sequence of quasi-steady states, and thus the membrane configuration should be determined by the balance of elastic force and pressure forces across the membrane interface. If the pressure difference across the cell membrane remains constant, the local tension or compression force is inversely proportional to the magnitude of local curvature K. It is expected that the majority of the membrane is under the tension mode ($K>0$), but the cone-shape membrane around the penetration point has a compression mode ($K<0$). This is a rough estimation by only considering the membrane curvatures. The detailed future

calculations should involve flow stress and membrane elasticity in an integrated framework.

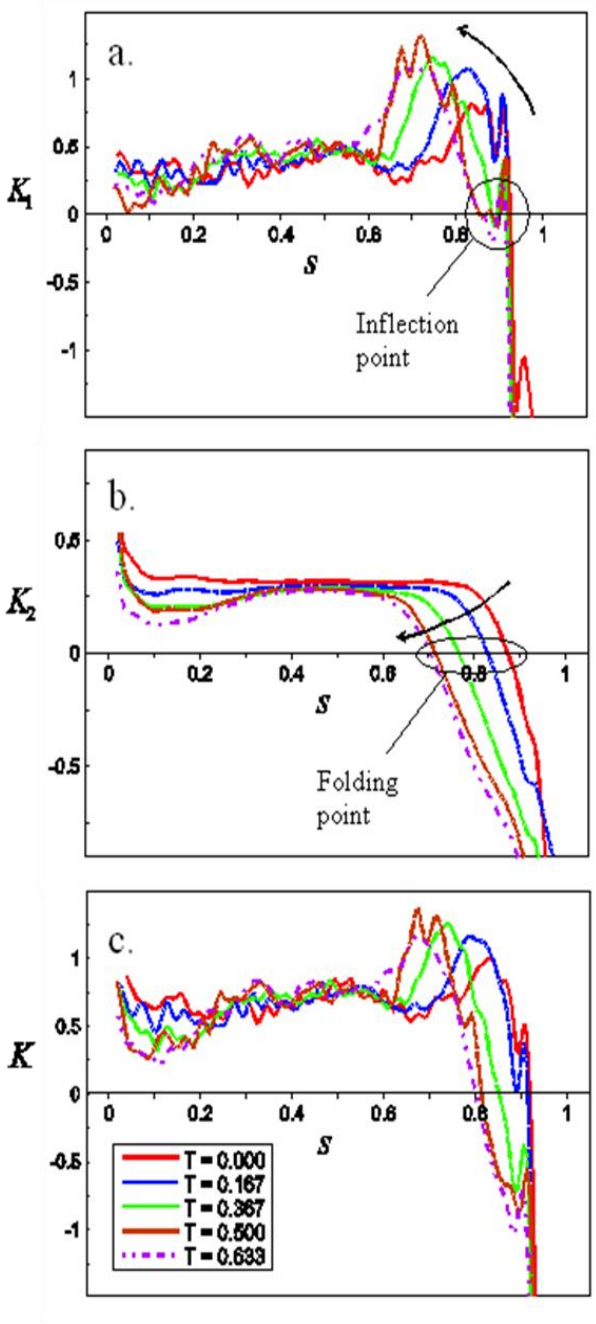

FIGURE 2.9: Evaluation of curvature a. K1, b. K2 and c. K for each profile in Figure 2.7.

From a number of practical observations the following correlation is extracted. The most effective membrane piercing occurs when the folding takes place at $s = 0.8$. The membrane tension level which corresponds to this feature is yet to be analyzed and validated further. Nevertheless this study encouragingly points out that there is a repeatable property (membrane curvature) which declares the desirable starting instant of the piercing (or rotational oscillations). It forms a trigger for the automated start of the Ros-Drill© operation.

Nevertheless, the described procedure, offers only a strong assessment in terms of mechanical validation for the initiation of rotational oscillations. In real practice, where the measurements are done in-situ, the curvature determination would delay considerably the overall performance. For the purpose of the current work, it is decided to keep the curvature determination as the theoretical background for the geometric feature that will define equally precisely but faster the onset point for the cell membrane to be pierced.

2.1.2 USING RADIAL DEFORMATION OF CELL MEMBRANE

In this method, the decision for the proper instant to initiate the Ros-Drill© oscillations is made by measuring the radial deformation of the membrane. The consideration for this selection involves the time constraint. Typically a conventional manual ICSI trial takes approximately 3 seconds from the first contact of the injection pipette with the oocyte to its removal from the scene after injection. A piercing period is expected to be within 1-1.5 seconds. This duration does not include the secondary attempt to achieve piercing following a potentially

unsuccessful one. The method ***a*** proved to be time-wise prohibitive due to the relatively intense computational load [21]. This observation leads to the simpler method of using radial membrane deformations..

The specifications of the microscopic imaging hardware utilized for this development are the same as the previous section. The digital images in the live-stream consist of data in 8-bit gray level scale (from 0 to 255 numerically) where the lowest value corresponds to *black* intensity and the highest to *white*. As the images are delivered with a determined sampling speed (which is 30 fps in this application) the relevant image processing algorithms should be performed in real-time. Therefore, the computation time for each frame (if analyzed consecutively) must be less than 30 ms. The real-time-analysis requires real-time-features to be extracted, and thus the selection of these features is very important.

Measurement of the membrane deformation (r_d - radial deformation of cell membrane is based on monitoring the relative motion of the tip of the injection pipette with respect to a reference point (the pipette-oolemma contact point), which is identified on the cell membrane in the undeformed state (Figure 2.10). Axial deformations can be measured in real time in contrast to Method ***a***. Once r_d approaches a reference value given by the user, the digital control activates the rotational oscillations of Ros-Drill©. The distance r_d is monitored using a tip-tracking algorithm to be described later in the text. As demonstrated in the earlier investigations [17-18], this monitoring can be executed in real time. This method is much more efficient and timely than the curvature-based procedure *a*. It forms the core objective in this paper. The initiation procedure for rotational oscillations

is the first step towards a comprehensive automation of the novel Ros-Drill© ICSI process. Detailed explanation on the image processing and decision algorithms is given in the following sections, as well as the results from the implementations.

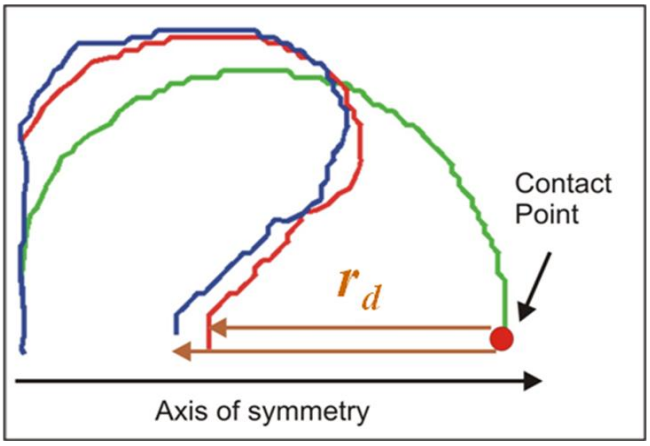

FIGURE 2.10: Radial deformation of cell membrane

- IMAGE PROCESSING

The microscope images are represented by a 240x352 matrix which contains the grey level intensities from 0 to 255, referred to as 'intensity levels'. The visual feedback-based automation procedures aim to reduce human intervention in the repetitive but critical tasks; it increases the computer participation without compromising the performance quality of the aimed task. Such replacement must be performed in real time and must consist of a reliable algorithm that is capable of evaluating the incoming video stream to extract valuable information. A small computational delay in the execution of the algorithm may be tolerated as long as it does not hamper the desired bandwidth

characteristics of the subsequent motions. From the typical experiments it is observed that the average axial speed of the pipette is 50 μm/s, during which it is intended to resolve 3 μm advancements (about 3 pixels at 20X magnified image). This resolution implies that triggering the start will come with a deviation of 3 pixels (~4% error corresponding to the oocyte with the diameter covering 80 pixels). This requirement also corresponds to about 16 fps image processing speed, implying that the processing is done every other frame to keep real-time display. The current image handling capabilities fulfill this requirement.

The first step to automate the Ros-Drill© technology consists of determining automatically the instant in which the drilling action should start to pierce the oocyte and consequently inject the sperm head into the cytoplasm. To reach this level of automation, the following stages of the algorithm are implemented over the live stream of images in a typical ICSI trial: 1. Binarization: Grey level threshold (called '*threshold*' for the rest of the text) is determined, and the frames are binarized accordingly, 2. Contact point determination (on the oocyte), 3. Pipette tip detection before engagement with the contact point, and 4. Pipette tip tracking after engagement with contact point to determine the amount of membrane deformation. All these routines are vision-feedback type and they can be categorized in two groups: off-line and real-time.

- OFF-LINE ROUTINE, THRESHOLD DETERMINATION

Before starting the on-line (real-time) work, extracting background information is important. This is done by assuming that the microscope

illumination and magnification settings are unchanged for a series of ICSI trials. The key information in this category consists of the grey-level threshold value *Th* and the average diameter d_0 of the oocyte in terms of pixels counts. The *threshold* value facilitates an appropriate binarization of the gray-level images, and the oocyte diameter is stored as a reference to compare with the pipette advancements into the cell. The oocyte diameter is determined by the routine simply counting the pixels between two diametrically opposed points on the membrane. This diameter is assumed to remain the same during a set of tests.

Threshold determination is of great interest for binarizing images in many image processing techniques [13]. There exist many ways to find a proper threshold value depending on the nature of the images and the accuracy of the expected results. In this case, the images contain several objects in the field of view, i.e., oocyte and micropipettes (Figure 1.1). The edge of each object shares similar intensity values (Figure 1.4 and Figure 2.11). Thus a simple procedure is developed to extract a threshold value to be used throughout the experiments. The calculation is done automatically with minimum engagement from the user. First a small rectangular window $\boldsymbol{w}$ containing the tip of the injecting pipette (Figure 2.11a) is selected manually over a static (unperturbed) image of the experimental set up. This window is described by a matrix of *r* rows and *s* columns of intensity values.

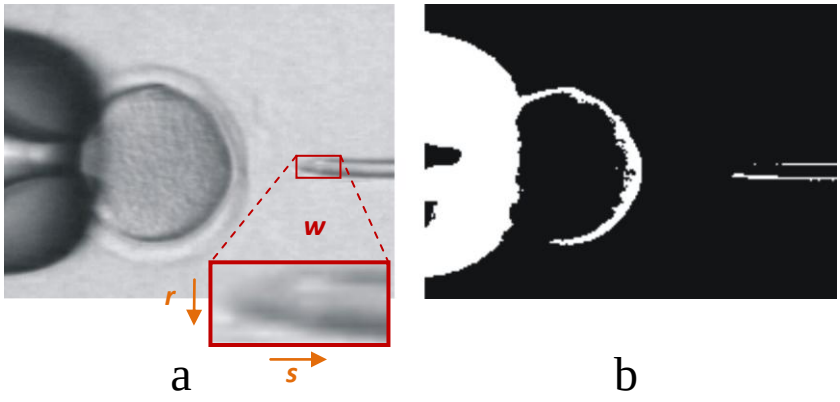

FIGURE 2.11: a. Window ***w*** and b. Binarized Image

Knowing that the darkest pixels with the smallest intensity values in window ***w*** represent the borders of the injecting pipette, a two-step scheme allows the identification of the *threshold* value: *i)* the minimum *intensity* value from each row of ***w*** is extracted and stored in a vector named ***th***, *ii)* the *average* of ***th*** components is used for the binarization threshold, *Th*. The algorithmic procedure is summarized as follows

$$\begin{aligned} &for\ i = 1\ to\ r \\ &\quad th\ (i) = \min\ \{I(i, j),\ j : 1..s\} \\ &end\ \ for \end{aligned}$$

$$Th = \frac{1}{r}\sum_{i=1}^{r} th(i)$$

Any intensity level below *Th* is treated as an indicator for an object (like the pipette edge), and those values above the *Th* are taken as the background. This logic is applied to the entire image frame (240x352) next. For ease of visualization during the developing process the negative (or conjugate) image mask is created, in which background is represented with *black* (binary value 0)

and foreground with *white* (binary value 1) for the entire frame including both pipettes and the oocyte. The binarized mask is called *BI*.

$$BI(i,j) = \begin{cases} 1 \; if \;\; I(i,j) \le Th \\ 0 \; if \;\; I(i,j) > Th \end{cases} \tag{9}$$

where *BI(i,j)* is the intensity value of pixel at position *(i,j)* in the conjugate binary image and *I(i,j)* gives the gray intensity value of the pixel at position *(i,j,)*, where *i* and *j* indicate the rows and columns respectively. The *BI* mask carries all the necessary features of the image (Figure 2.11b) for ensuing the real-time phase of the algorithm, yet it is considerably simple due to its binary nature (Figure 2.11b).

- REAL-TIME CONTACT POINT DETERMINATION

Differently from "off-line" procedures, this phase of the routines (2 to 4) is repeated for each oocyte. Some of the operations (3 and 4) are performed in real-time as the piercing is performed. The aim is to monitor the axial displacement of the pipette tip with respect to the oocyte membrane. Over the in-situ live-stream images, automated Ros-Drill© operation starts at a certain oocyte deformation.

The first geometric feature to be found on each oocyte membrane is the "contact point", where the injecting pipette is expected to engage during piercing. Finding this point serves as reference for the following procedures (3-4). First, an image without injecting pipette in the field of view is binarized using Eq. (9). Assuming the area of possible location for the contact point, a window ***R*** is considered as depicted with the red rectangle in Figure 2.12, which is defined by

the location of its upper-left corner (p_x,p_y) with predetermined width f and height g (both in pixel counts). Second, a row sweeping process takes place within ***R***. The sweeping is performed from right to left and from the top row down. The small routine given below results in J and I values to represent the horizontal and vertical position of the contact point within ***R*** (Figure 2.12).

$$
\begin{aligned}
&for\ i = p_y\ to\ p_y + g && (top\ to\ bottom)\\
&\quad for\ j = p_x + f\ to\ p_x && (right\ to\ left)\\
&\qquad if\ \ BI(i,j) = 1\quad ,\quad l = i\quad white\ pixel\\
&\qquad\quad if\ \ j < J\ ,\quad I = i\ ,\quad J = j\quad end\ if\\
&\qquad end\ if\\
&\quad end\ \ for\\
&end\ \ for
\end{aligned}
$$

Here, (p_x,p_y) is the location of the upper-left corner of ***R***. Once this evaluation finishes, the contact point is located on the row I that delivers the smallest distance from right edge of ***R***. The expected contact point appears as:

$$
\begin{aligned}
cp_x &= p_x + f - J\\
cp_y &= p_y + I
\end{aligned}
\quad , \tag{10}
$$

which establishes the initial engagement point between the pipette and the oocyte.

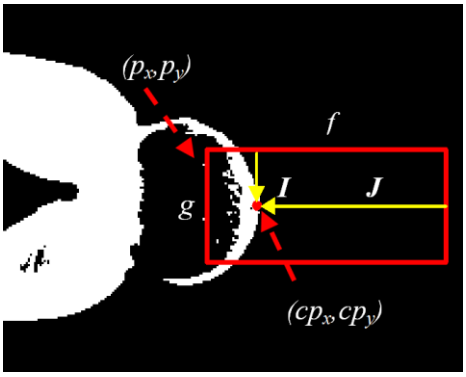

FIGURE 2.12: Detecting the contact point

- REAL TIME TIP DETECTION BEFORE ENGAGEMENT WITH THE OOCYTE

The tip location of the injecting pipette is identified by *(x,y).* This point freely moves under the control of a pipette manipulating mechanism (for the moment manual guidance is used).

The image is divided into two partitions by the vertical green line passing through the contact point (cp_x,cp_y) in Figure 2.13.

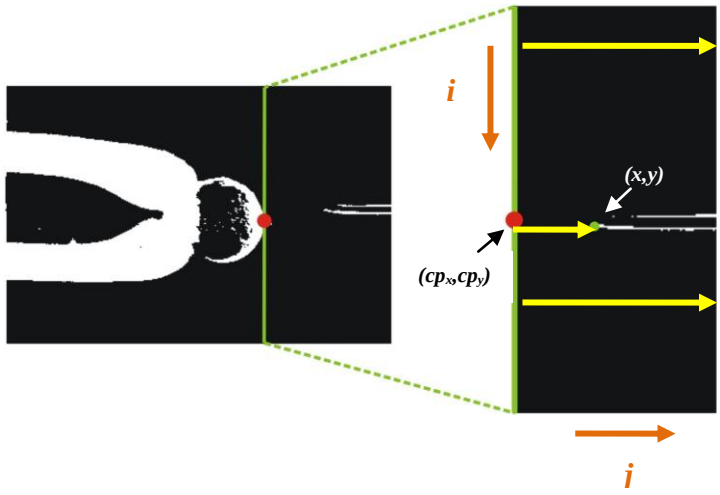

FIGURE 2.13: Partition to the right of contact point

The partition on the right is used for searching the tip characteristics. A recursive algorithm scans pixels from left to right, one row at a time. Since the pipette can enter the field of view from the right-most edge of the frame, the algorithm tries to find the white pixel that has the minimum distance from the green vertical edge. This very first white pixel represents the tip of the injection pipette. This sweeping logic is similar to that for the contact point detection,

except that this is performed for the entire field of view of the partitioned image on the right. The routine is:

$$
\begin{aligned}
&for\ i = 1\ to\ 240 \\
&\quad for\ \ j = cp_x\ to\ 352 \\
&\qquad if\ \ BI(i, j) = 1 \qquad first\ white\ pixel\ on\ row\ j \\
&\qquad\ if\ \ j < J, \quad j = j, I = i \quad end\ if \\
&\qquad endif \\
&\quad endfor \\
&endfor
\end{aligned}
$$

where (*i*,*j*) are the coordinates of the pipette tip in terms of the pixel counts within the partitioned image, defined as:

$$
\begin{aligned}
x &= cp_x + J \\
y &= I
\end{aligned}
\quad , \tag{11}
$$

The above algorithm is repeated in real-time for tracking the pipette tip motion. Due to the computational delays and the nominal speed of pipette motion discussed earlier, every other frame is processed (that is, 1/15 sec sampling period for this routine is given including the graphics display). The goal here is to accurately track the tip while the injecting pipette is driven towards the contact point. Once engaged, the analysis changes to another algorithmic logic as it is presented next.

- REAL TIME TIP DETECTION AFTER ENGAGEMENT WITH THE OOCYTE

This is the most critical stage of the operation as the automated initiation of Ros-Drill© rotations would take place. The pipette tip tracking algorithm has to

be modified because the logic presented earlier for the isolated tip cannot be applied. Figure 2.14 shows how the pipette tip joins the cell membrane once it engages at the contact point, however, the deformed shape of the oocyte can be effectively utilized for tip tracking in this phase of the operation.

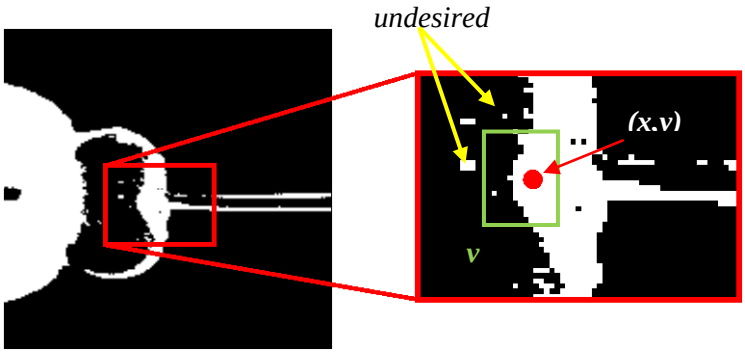

FIGURE 2.14: Binary image once the deformation starts

The relevant algorithmic development is explained in several aspects next. First, it is assumed only the horizontal movement of the injection pipette in this phase (in practice this is typical). Consequently the analysis can be constrained to a narrow region within the immediate vicinity of the pipette tip of the previous step (Figure 2.14). The digital process is confined within a neighborhood of 20x15 pixels, called window ***v***, centered around the previous tip position *(x,y)*. Its upper-left corner is located at *(x-7,y-10)* and the lower-right corner at *(x+8,y+10)*, which forms the green rectangle in Figure 2.14 (The size of ***v*** as well as the location of its corner may vary depending on the resolution of the camera). Second, image enhancements are performed as follows. Within the region ***v***, the zona pellucida, cell membrane, injecting pipette, and the oolemma (membrane) appear as white (foreground objects), as well as some undesired irregularities in

the cytoplasm in the conjugate binary image. These small objects must be deleted to prevent a false tip location. To do this, a neighborhood pixel evaluation procedure is implemented: *i)* every immediate neighborhood of a white pixel in ***v*** is evaluated; starting in the upper-left corner of ***v***. *ii)* All the white pixels are labeled along with their connectivity. If surrounding neighbors of the current pixel are white, they belong to the same objects (cluster). The current white pixel, as well as its neighbors, is given a label (number). If any two white pixels are not adjacent, they belong to separated clusters. *iii)* The cluster labels are stored in a matrix ***c*** (20x15), in the same position of the pixel that created it (Figure 2.15a). *iv)* A vector ***e*** is created whose size is equal to the number of white clusters in window ***v***. Vector ***e*** stores the number of pixels in the corresponding clusters. For instance, the number stored in the 4-*th* position of ***e*** corresponds to the number of white pixels in cluster 4 (Figure 2.15b).

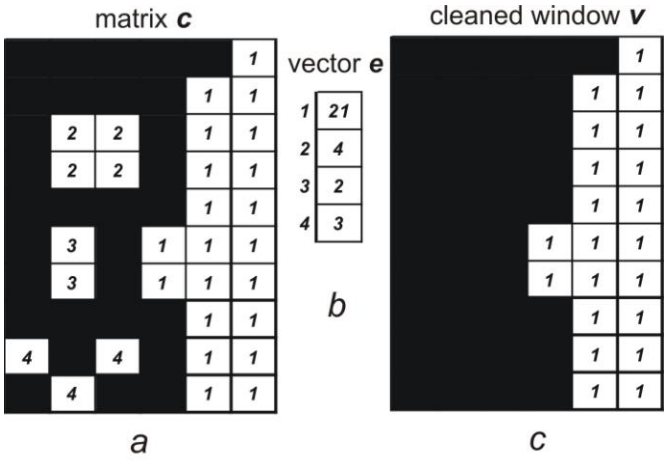

FIGURE 2.15: Partial view of window ***v***. a. Label matrix ***c***, b. Vector ***e*** and c. after deleting small objects

v) Once all the white pixels in window ***v*** are accounted for, those clusters with fewer pixels than a minimum size are eliminated. In this work this minimum size is taken as 20 pixels considering that window ***v***, after injection pipette engages the oocyte, will have more than 20 rightmost front pixels in its biggest cluster. This cluster is kept as the starting point of this segment of the routine (very similar to Figure 2.13). From this point forward a recursive algorithm is applied to find the tip while it is pushing the membrane into the cell. *vi)* Finally, the left-most white pixel inside the cleaned window ***v*** is determined to define the current coordinates of the tip. This process starts from the right wall of ***v***, and it is algorithmically identical to the pipette tip detection before engagement at this last leg. Considering that in the previous frame the pipette location is (x_p,y_p), the current coordinate of the tip is expressed as:

$$\begin{aligned} x &= x_p - 7 + I \\ y &= y_p \end{aligned} \tag{12}$$

Here, the number 7 comes from the location of window ***v*** at the upper-left corner and y_p is equal to cp_y, the y coordinate of the contact point (This value may change depending on the resolution of the camera). This algorithmic structure tracks the pipette tip in real-time after the pipette engages with the contact point. In-situ calculations of the radial deformation of cell membrane follows, as

$$r_d = \left| x - cp_x \right|, \tag{13}$$

At the final stage of the algorithm a comparison between the present radial deformation r_d of the oocyte membrane and a desired deformation, d_d (in pixels counts), is made. This user defined quantity is typically a percentage of the nominal oocyte diameter, d_0, which is readily converted into pixel counts under given microscopic magnification rate. Once the condition $r_d = d_d$ is reached the algorithm generates an automatic pulse to initiate the rotational oscillations in the Ros-Drill© device. In the tests this pulse is generated via the audio card of a laptop computer. The pulse has amplitude of 200 mV and duration of 0.0625 seconds. This small signal is amplified using a low power Op-Amp with power supply of 24 V, which is then fed into the controller that operates Ros-Drill© [11]. This completes the automated starting procedure of Ros-Drill© with minimal user interface and in a repeatable fashion. This automated process is implemented in such a way that if the piercing does not occur in the first attempt, the user is given a second chance.

The CPU time in this real-time image processing routine is less than 200 ms. This is an acceptable delay for a realistic ICSI test allowing the specialist to monitor the injection properly. Two test cases are presented in the results chapter to demonstrate the performance of this automated Ros-Drill© operation.

2.2 ROTATIONAL MOTION TRACKING

In the α prototype: The existing Ros-Drill© micro-injector prototype employs a PLC (Programmable Logic Controller) as the digital controller, which has a maximum control sampling speed of 1000 Hz. This constraint limits the controlled frequency (f_d) to 500 Hz. The current DC motor that moves the pipette has an optical encoder with 512 lines and quadrature signature capability which results in a sensor resolution of 0.176 deg [11]. Most recently reported ICSI tests use injection pipette oscillations at 0.2 deg amplitude (A_d) and maximum frequency of 500 Hz. These preliminary reports claim that Ros-Drill©-assisted ICSI results in embryo survival, embryo development, birth, and weaning rates comparable to those of piezo-assisted ICSI using mercury [12]. Although these biological results are very promising, the trajectory tracking performance of the α prototype is not satisfactory because of the following shortfalls in this setup:

- Low-resolution of position sensor. For instance, if the desired amplitude of the intended oscillations is 0.2 deg, there are only two steps of encoder reading (maximum) within the intended peak-to-peak stroke, implying a very coarse sensing capability (Figure 2.16).
- Low sampling rate (f_s) of the PLC, which is 1000 Hz. For instance, if the desired frequency was 700 Hz instead of 500 Hz, the sampling rate must be at least 2100 Hz [22].

Combination of these obstacles create undesirable tracking performance over a given harmonic trajectory, in particular for higher frequency ranges. Hence, the enhancement effort presented in this thesis is conducted. The new

structure aims the following features which are more demanding: satisfactory tracking performance of a harmonic trajectory with smaller amplitude (e.g., 0.2 deg) and higher working frequencies (400-700 Hz) using a **smaller, inexpensive and user-friendly** control facility. Along with the visual control of the Ros-Drill© initiation, this work presents the design of a control system, and its hardware-software aspects satisfying these requirements.

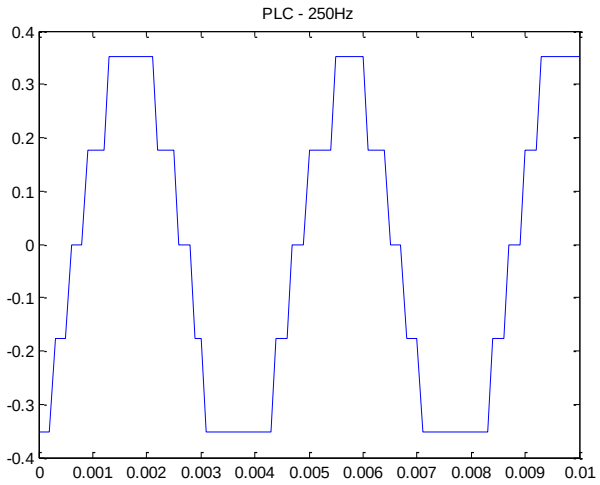

FIGURE 2.16 Rotational oscillations for α prototype, (f_d=250Hz) .

2.2.1 HARDWARE ENHANCEMENT

The improvements made on Ros-Drill© involves all the stages in hardware design. The selection of a different controller required the use of additional concepts and elements to guarantee an adequate control implementation. In Figure 2.17 the general scheme for the new version is presented. Each one of the stages in the design is explained in detail next. Figure 2.18 shows the PCB cards for the new assembly.

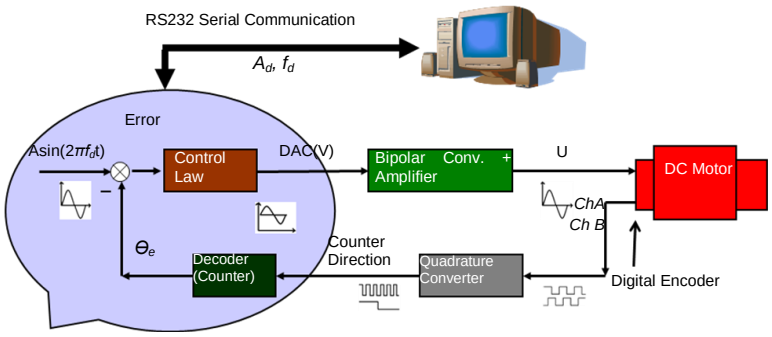

FIGURE 2.17: Scheme of β Ros-Drill© - Hardware Implementation

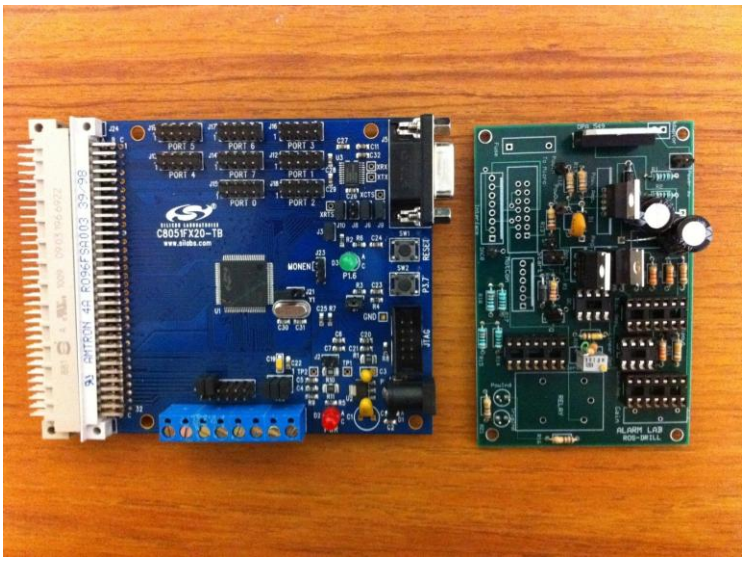

FIGURE 2.18: PCB Cards. Left, Microcontroller. Right, Driver card

The component description of the original Ros-Drill© was presented in the earlier publications [11-12], which are specific to the device used during initial

experiments. The detailed component layouts and connection diagrams are also provided in the APPENDIX I. The key improvements are listed below:

- NEW MOTOR WITH A BETTER MOTION SENSOR

A DC motor is used for motion generation. The motor selection is based on the frequency bandwidth needs and the space available. The motor should be fast enough to generate high frequency oscillatory motion and also small enough to fit in Ros-Drill© casing. Overall weight of Ros-Drill© is constrained with load carrying capability of the micromanipulators. Small weight, short mechanical time constant and certain level of power output are important mechanical requirements for the motor selection. Necessary calculations are as follows.

$$\begin{aligned} T_m &= J\ddot{\theta}_d + B\dot{\theta}_d \qquad \theta_d = A_d \sin \omega t \quad \omega = 2\pi f_d \\ P(t) &= T_m(t).\theta_d(t) \qquad P_{req} = \max(P(t)) \end{aligned} \tag{14}$$

where T_m is motor torque, J and B represent moment of inertia and viscous friction coefficient respectively. θ_d is angular position of the pipette holder with amplitude A_d, and frequency f_d. $P(t)$ is the instantaneous mechanical power. The maximum value of it is P_{req}, which is the power level required by the system. The maximum power demanded from the motor is found by (14) about 7.5 W for generating a sine wave with an amplitude of maximum 2 degrees (although the targeted desired amplitude is ten times smaller – 0.2 degrees). A motor satisfying these requirements mentioned above is selected among commercially available motors. However, as it is intended to keep desirable small dimensions for the proper set

up with the micromanipulator, the DC motor should have an embedded encoder to facilitate its placement. This condition narrows down considerably the range of available DC motors which comply with the conditions previously described.

Faulhaber 2342012CR DC motor is selected as an appropriate device with the matching mechanical dimensional requirements and power demand of the rotational system. The diameter of the motor is d_m = 22 mm and the length is l_m = 42mm. The shaft diameter is d_{sh} = 3 mm which is less than the pipette holder diameter. The axially flexible coupling is also a bridge between two different shaft diameters. On the other side of the motor shaft, the embedded encoder is located. The output power of the motor is P_o=17 watts and mechanical time constant is τ_m = 6ms. Rotor inertia of the motor is J_m = 5.7 gcm^2 and maximum angular acceleration is α_{max} = 140 10^3 rad/s^2.

The reference signal for purely harmonic rotational oscillation of the pipette is again $A_d\sin(2\pi f_d t)$ as in (Eq. 1) ,where A_d is the amplitude of the oscillation (degrees) and f_d is the frequency (Hz).

For the nominal desired amplitude of A_d = 0.2 deg, the new encoder with resolution of 0.09 deg detects only four steps for one peak-to-peak stroke. This coarse measurement introduces considerable sensing errors (as much as 0.09 degrees which is 45% of the nominal amplitude, A_d). Although the newly adopted sensor is twice as much sensitive as the old encoder (1000 lines instead of 512), they still render the error signal meaningless for an effective closed loop control. Sensing shortfall results in a very crude determination of higher order derivatives of the measured quantity which ultimately prevents the adoption of traditional

methods to design the control system, such as pole placement, repetitive control, loop shaping and so on. To overcome this difficulty an adaptive feedback routine is introduced which, in essence, tunes the control logic based on the target operating frequency. The proposed scheme is explained in detail in Zhang et al. [25]. It is important to clarify that this is the best option for an encoder in terms of size, resolution and costs demanded by the application.

- MICROCONTROLLER C8050 REPLACING THE PLC

In the first Ros-Drill© version, the controller unit corresponded to a PLC (Programmable Logic Controller) with features described as follows: I/O digital ports, voltage range from 0 to 24 Volts, sampling frequency of 1000 Hz, A/D and D/A embedded converters. These allowed the creation of oscillatory profiles [11-12] that were tested in biological trials. Nevertheless, it was concluded that the higher the frequency the better the response of the cell membrane to the rotational movement, leading to better survival rates. The sampling frequency of the PLC (1000 Hz) is too low to have an accurate tracking of rotational motion with high frequencies such as 500Hz. This happens to be the critical feature to be considered for the selection of the microcontroller used in the upgraded version of Ros-Drill©.

In order to increase the operating frequencies up to 700 Hz (and possibly 1000 Hz) the sampling speed must be increased by at least 10 fold with respect to the current limitation of the PLC. To fulfill this need a powerful but inexpensive and

commonly used microcontroller, C8051F120 (manufactured by Silicon Labs) is selected (Figure 2.19).

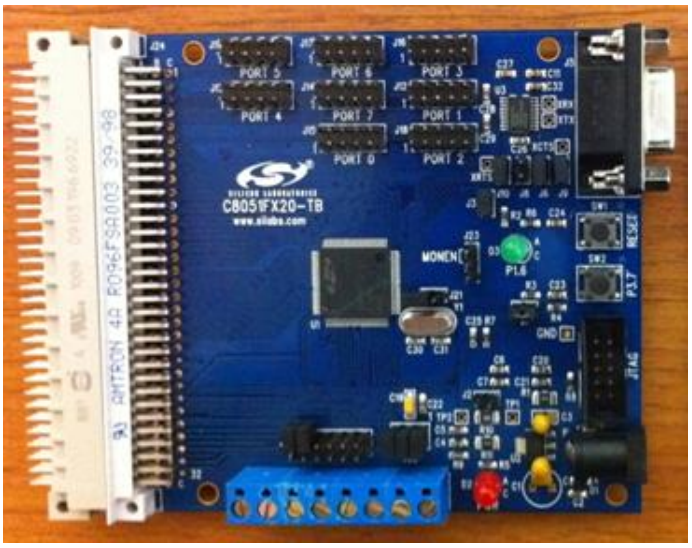

FIGURE 2.19: Microcontroller C8051 card

Its clock speed can reach up to 100 MHz. A comfortable 10 KHz SISO (single input-single output) control sampling rate can be achieved with 71.8 μs of total loop time. This loop time mainly includes sensing, control logic evaluation and D/A conversion.

As the selected microcontroller works in a much different range of output voltages values (up to 3.3 Volts) instead of 24 Volts (PLC), and delivers only positive signals, the driver card had to be redesigned to satisfy the new motor demands. Specific modifications will be shown later in the text.

In the remaining part of this section we wish to present some of the peripheral devices which are newly introduced in the micro-controller support.

a) Linear optocoupler: The motor usually requires currents slightly higher than 1 Amp for regular conditions of work within the desired frequency and amplitude ranges. In the first version, this problem was tackled by simply building a driver card utilizing a power amplifier. This amplifier took the signal coming from the PLC and conveyed it into the motor supplying the required demand of current imposed for the motor. In that case, no problem arose between connecting the PLC directly with the power amplifier, since that kind of controllers are quite robust and intended for high power applications. Nevertheless, for the new microcontroller the situation is different. This controller is a small chip with extremely broader processing capabilities, but limited power demands and current handling ability. Therefore it must be isolated. To achieve this, a linear optocoupler is used, which functions as a safe bridge and translator of the low-power analog output of the microcontroller into the driver card that controls the motor. In Figure 2.20 a schematic of the driver card can be seen. Again, the details can be found in the connection sketches of APPENDIX I.

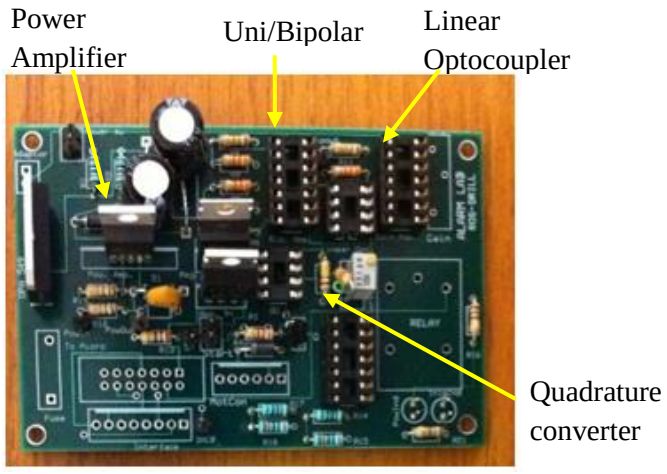

FIGURE 2.20: Driver card

b) Unipolar to bipolar converter

There is another important difference with respect to the first version. The PLC could deliver positive and negative voltages because it has a converter already built in. The C8051 cannot work with two-polarity voltages. Therefore the peripheral circuit (embedded in the driver card) must compensate this problem (Figure 2.20). Here, the Unipolar-Bipolar stage takes the output of the linear optocoupler as input. This signal is an all-positive alternate voltage within a small range (0-3.33 V) centered at 1.65 Volts (Figure 2.21 left). This implies that this signal is output by the microcontroller with a positive offset that if fed without conversion into the motor would make it rotate in addition to the expected oscillations. This is obviously a very critical problem, since the key of Ros-Drill© procedure is its clean and accurate oscillations with no shaft rotation. By using a couple of operational amplifiers and an adjustable voltage source (Figure 2.20), this offset can be reduced to zero achieving a pure AC signal (Figure 2.21, right).

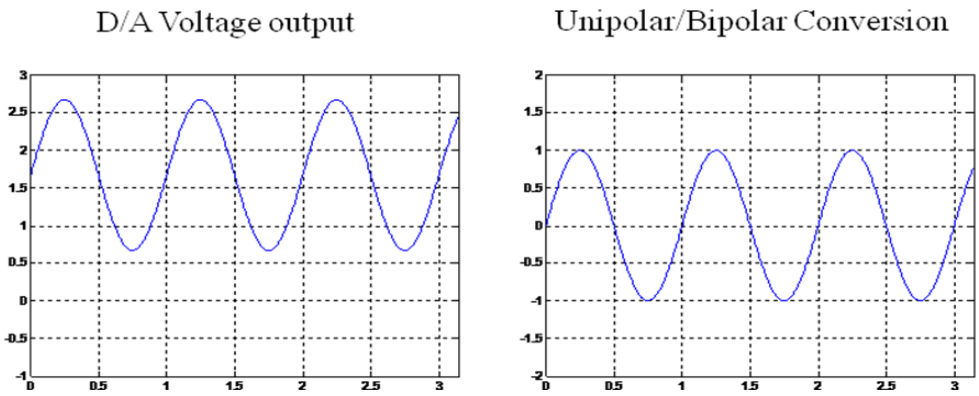

FIGURE 2.21: Unipolar to Bipolar voltage conversion

c) Encoder reading – quadrature converter

The last important peripheral has to do with the feedback reading. It was just discussed that a new encoder was also selected to improve the quality of the feedback measurements. However, this encoder works in quadrature mode, offering two signals to be interpreted as the shaft position in a specific direction. These two signals come from the light blocking of two transmitters, induced by a marked board containing the number of lines that define the encoder resolution. These transmitters are separated 90 deg. To get the current position of the motor, an evaluation of two things must be implemented: 1. the number of changes of state, either low to high or high to low must be counted. This gives the amount of displacement and 2. It must be acknowledged which signal is ahead and which behind in order to determine the direction. This analysis is not complex, but in terms of computational cost for the microcontroller it implies some time waste. Currently, in the market, there exist some chips that make the conversion of these quadrature signals into two simpler signals that reduce considerable the time of execution. These are known as quadrature converters (Figure 2.20). Its inputs correspond to the two quadrature signals just described and the outputs are defined as: 1. Signal containing the number of steps moved by the motor (CLK) and 2. Signal representing with two digital levels either clockwise or counterclockwise direction (UP/DN) (Figure 2.22).

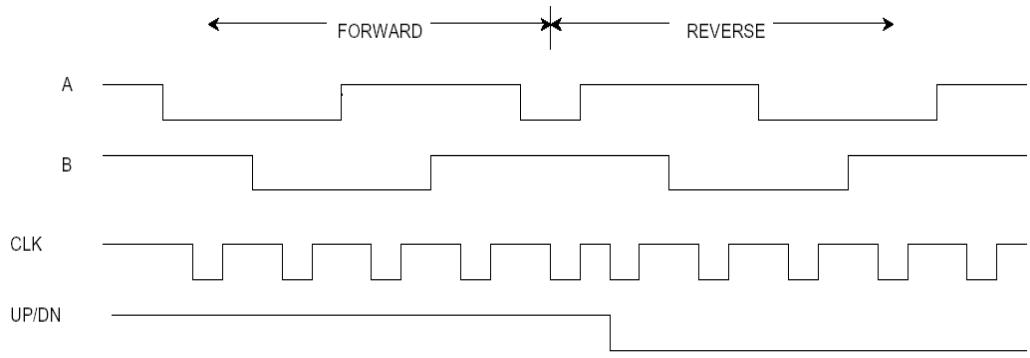

FIGURE 2.22: Quadrature conversion

2.2.2 SOFTWARE IMPROVEMENT

A SISO sampling speed of 10000 Hz is experimentally validated on the new microcontroller as a comfortable operating speed with the computational load as described later being in the loop. This increased sampling speed eliminates the constraint of samples per period to guarantee having a good control. However, the coarse sensing capability is still remaining. Furthermore, for the higher range of operating frequencies, a new problem arises: Digital representation of the desired trajectory, θ_d, as defined in Eq. (1).

- DESIRED TRAJECTORY GENERATION

This is the departure point in the program improvement. Based on the user inputs (desired amplitude A_d and frequency f_d) the microcontroller creates a digitized version of the desired trajectory to be followed by the pipette tip. In this process an interesting issue arises due to the microcontroller sampling rate (f_s). To generate θ_a the digitized version of θ_d two alternatives were considered:

a. Firmware evaluation of the harmonic trajectory in each control sampling instant. A C++ routine is used for this, which evaluates a sufficient number of terms in the series expansion of a sinusoidal function and generates the digitized desired path.

b. A priori-calculated sine-wave template, a sine function, θ_a is evaluated at the sampling intervals and stored for one cycle. They are called in sequence for each cycle and the cycles are stitched together as the control proceeds.

Figure 2.23 shows the comparison of time consumption between the two different methods for each part of the control loop, including the digital construction of θ_a, reading the actual position θ_{enc}, computation of control command and DAC (D/A converter) output. The generation of θ_a using method ***a*** takes 64.3 μs which forces the control loop to complete in 134.8 μs, which is larger than the selected sampling period 100 μs. Therefore the method ***a*** is impracticable. Method ***b*** proves to be the only choice, which consumes only 1.3 μs for generating θ_a and the control loop takes approximately 71.8 μs sparing about 30% of the sampling period to achieve resetting for the next loop (book keeping in the microcontroller). It is clear that this scheme comfortably supports 10 KHz sampling rate.

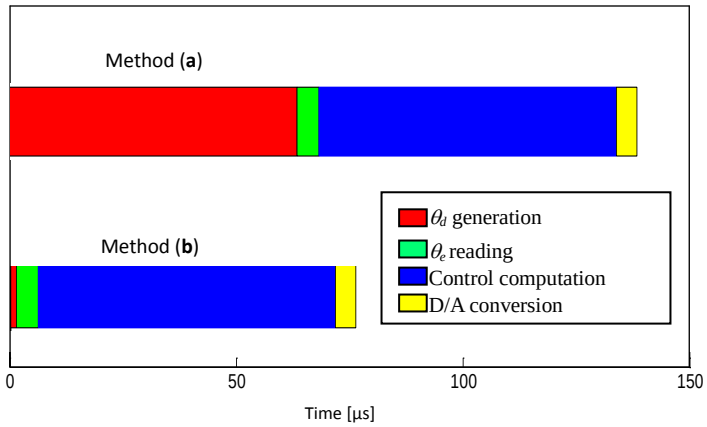

FIGURE 2.23: Comparison of different methods of θ_a generation: A. Using Firmware, B. Using pre-calculated template

In the preferred method ***b*** harmonic desired trajectory generation presents an interesting problem: As mentioned earlier, this procedure cannot produce the desired frequency exactly due to its dependence on the sampling period. The number of sampling instants per cycle, N_p, which is used to form the harmonic wave template, is

$$N_p = floor(f_s / f_d) \tag{15}$$

Therefore the actual period of the template becomes $N_p \cdot T_s$, which is always smaller than the intended period (as a small segment of T_s is dropped out, due to the floor function). The corresponding frequency becomes

$$f_a = (N_p \cdot T_s)^{-1} \tag{16}$$

which is always larger than f_d , i.e., $f_d \leq f_a$. Notice that $f_d = f_a$ occurs only when f_s is integer multiple of f_d. For such cases $N_p = floor(f_s / f_d) = f_s / f_d$. In short, the procedure for the creation of θ_a is as follows:

1. N_p is determined as in Eq. (15).

2. For N_p sampling points the microcontroller evaluates the sine function and stores these values as the template for θ_a. The routine for this is simply stated as follows:

$$\begin{aligned} &for\ \ i = 1 to\ N_p \\ &\quad Sine\_template\ \ (i) = A_d \sin(2\pi f_a T_s \cdot i) \\ &end \end{aligned} \tag{17}$$

3. For N_p+1 points (including the starting i = 0 value) a harmonic template is completed. i= N_p+1 would again result in i = 0 starting point. The harmonic template is therefore called repetitively with practically no loop time cost. This computational benefit, however, brings a restriction to the set of achievable frequencies in the process.

This issue arises due to the jump variations in the floor function when N_p is determined. A graphical display is presented in Figure 2.24, the blue dashed line shows the scenario for f_a = f_d and the red solid stairs curve shows the mapping of f_d into f_a. From these two pieces of information, the difference between f_d and f_a is known. As f_d increases the difference increases. For the intended peak operating point f_d = f_a =1000 Hz introduces zero error, but for f_d = 920 Hz, f_a = 1000 Hz and the difference becomes f_a - f_d = 80 Hz, the largest. From the biological perspective, however, f_d is not selected with strict small increments and therefore this nuance

is not critical for the Ros-Drill© experiments. Therefore from this point on f_a is the objective frequency to be followed, not f_d. Indeed, the feedback control structure will function to enforce this.

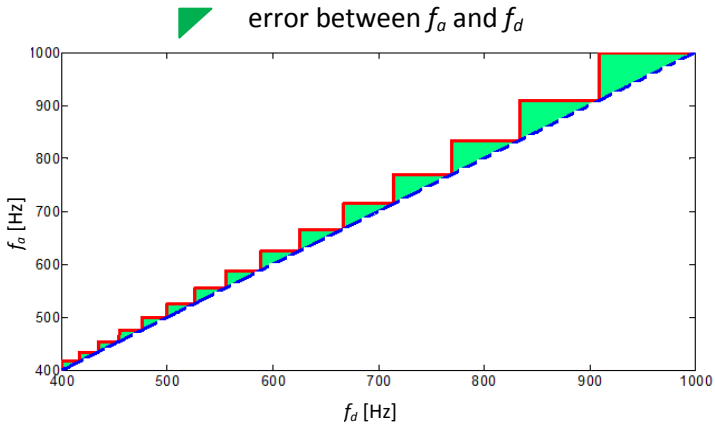

FIGURE 2.24: Discretization effect in Eq. (16) and the correspondence of f_d (Blue dashed line) and f_a (red solid line)

In Figure 2.25 an example for f_d = 600 Hz is shown. The template entails N_p =16 points (plus the starting zero), but a remainder of 400 from the division of Eq. (15) is there. From Eq. (17) the values for each point (sinusoid template) are found completing the sinusoid representation in one cycle. The control loop calls the values stored in the sinusoid template in sequence and repeats them after one cycle. The actual frequency f_a in this example is 625 Hz as opposed to 600 Hz.

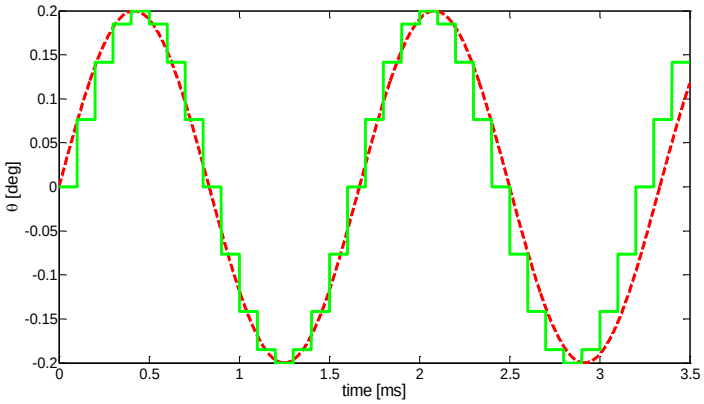

FIGURE 2.25: f_d = 600 Hz (red dashed line) and f_a=625 Hz (solid green discrete template), N_p=16

This variation, however, is not very critical as in biological tests, the Ros-Drill© frequency does not have to be created with precision but around a nominal quantity.

2.2.3 DESCRIPTION OF THE CONTROL

It is intended to deploy a conventional PID control law which overcomes these complications. This section presents the general scheme of a remedial novel approach, "adaptive hybrid control", developed concurrently by another researcher in Alarm Lab, Zhenyu Zhang [25].

In Figure 2.26 the relevant logic flowchart is presented. The user enters the key data, A_d (amplitude) and f_d (desired frequency) of the oscillations. Then θ_a with its corresponding f_a is generated and stored in a sine-wave template. In parallel, the routine selects the convenient control gain set for the given θ_d from an adaptive look-up table (Table 1).

f_d (Hz)	f_a(Hz)	K_p	K_i	K_d
400	400	4.5	8	0.0024
500	500	4.5	8	0.0036
600	625	4.5	8	0.0055
700	714	4.5	8	0.0070

TABLE 1: Frequencies f_d and f_a, and their corresponding control gains

Each working frequency f_d has its corresponding f_a and therefore its own PID gains set that delivers the best possible control signal for a smooth tracking as it will be seen in the next chapter. After the switch is activated (either manual activation or visual-feedback controlled, section 2.1.2), the control loop starts as follows: Actual θ_{enc} is detected from the encoder and subtracted from the artificially generated trajectory θ_a to obtain the error θ_e. Then, the error signal is treated by the adaptive PID control logic and the control signal is fed to the driver card.

The driver card converts the digitally generated control signal to analogue (D/A converter is within the C8051 microcontroller), which is later amplified. This signal becomes the command voltage to the micro motor. The control loop continues until the predetermined oscillation duration time T_d is over. In effect the oscillation lasts a predetermined time interval. This contrasts with the first Ros-Drill© version. In the developing process after increasing the frequency up to 500 Hz, the variable amplitude and fixed-duration profile (Figure 1.5) was changed to a fixed amplitude one with undefined duration (Figure 1.6). This duration was set manually by the specialist introducing uncertainty in the precise duration for the

cell membrane drilling. In the β prototype the duration can be set automatically by selecting it from a knob in the user-friendly prototype (Figure 2.27).

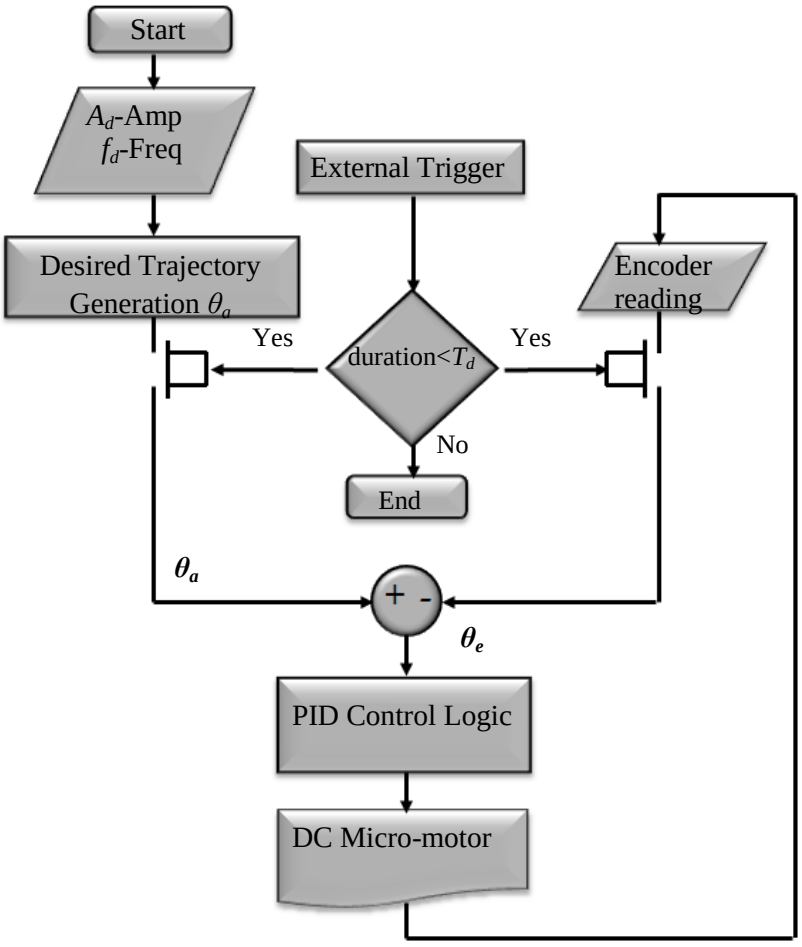

FIGURE 2.26: Flowchart of the controller program

There is also a caution implementation that allows the specialist to handle the PID selection without going into detail about the controller. One of the biggest contributions of the control strategy developed in the concurrent work [25] led to determine that the derivative gain is the one which contributes the most to the

amplitude quality. As the importance of Ros-Drill© prototype lies not only in its performance improvement but also in how friendly it is for the final user (specialist) to manipulate, a two light-led indicators are used to signal when an over or under-shooting of amplitude of feedback signal occurs. While the control signal is being generated with duration T_d a subroutine in the microcontroller scans for the average of the amplitude of the feedback signal [25]. As the feedback signal is represented as a discrete version of the desired trajectory, the monitoring routine will check the number of pulses per cycle to determine if over or under-shooting occurs (e.g., Figure 2.16). If the average exceeds a desired threshold the over-shooting light will turn on indicating the pipette is oscillating with slightly higher amplitude (Figure 2.27).

FIGURE 2.27: Ros-Drill© controller

Similar reaction occurs when under-shooting appears. In order to correct this problem, another knob (rotary switch) is included in the β prototype. Here, the specialist will correct the amplitude by increasing or decreasing the position of the knob, although internally, the microcontroller is adjusting the D gain based on a precise look-up table with gains for determined frequencies

3. EXPERIMENTAL RESULTS

The results presented in this chapter are divided into two parts: Visual feedback testing results and experimental and simulation results of rotational automation.

3.1 VISUAL FEEDBACK TESTING RESULTS

- IMPLEMENTATION OF TRACKING ROUTINE AND AUTOMATED INITIATION OF ROS-DRILL© ACTION

The algorithmic steps described in section 2.1.2 are performed on two different classes of tests on mouse oocytes. They differ in the declaration of the desired depth of penetration (radial deformation of cell membrane), d_d, for the start of the automated Ros-Drill© action. Based on the earlier experimental work, all of which required human interruption for the start of the Ros-Drill© action [11-12], d_d was taken as **55 and 60% of the diameter** of a free-standing oocyte, d_0. Out of a number of piercing tests we present two here (Figure 3.1) with d_d = 50 and 60 % of d_0. Both groups of attempts were observed to be successful for the membrane piercing phase alone, without the biological development studies.

In Figure 3.1, the first frames show the pipettes before the engagement with oocyte. The middle frames are at the time of the automated start of the Ros-Drill© oscillations (when piercing takes effect). And the final frames show the spring-back action of the pierced oocyte due to the membrane relaxation while the pipette is in it. From the piercing automation aspects this observation is sufficient, pending further biological tests which the author is currently engaged in.

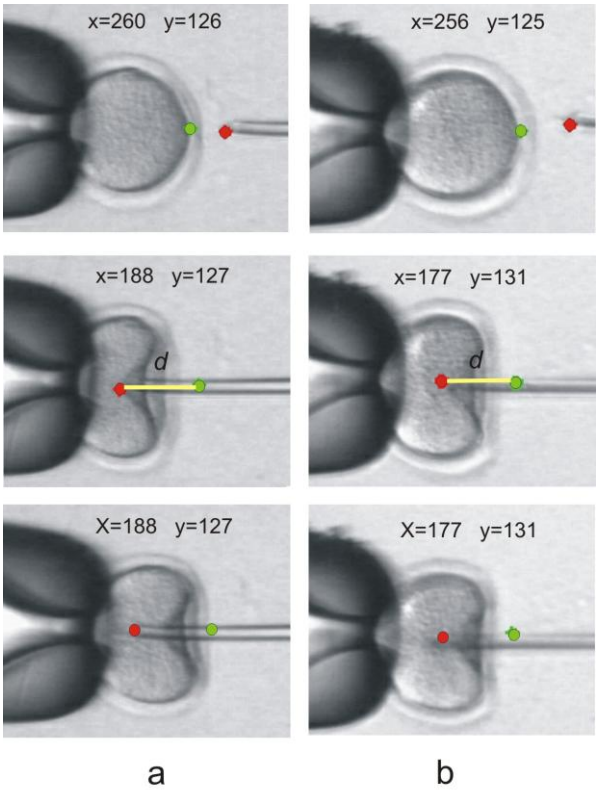

FIGURE 3.1: Tracking the injecting pipette, automation of Ros-Drill©, a. 60% and b. 55% of radial deformation.

- OOCYTE CURVATURE STUDY VERSUS THE CELL DEFORMATION APPROACH

The visual feedback of cell deformation amount was used earlier in a previous study [21]. Instead of monitoring the radial deformation r_d of the oocyte, it was implemented another geometric characteristic of the process: the total curvature variations analysis (Section 2.1.1). Next a comparison between the two techniques is presented.

In reference to Figure 2.6, the total curvature on the axis-symmetric oocyte is defined for every point *p* from *A* to *B* along the arc length *s* in terms of the two principal radii R_1 and R_2 as:

$$K = 1/R_1 + 1/R_2, \tag{18}$$

where R_1 is the local radius of the oocyte membrane at *p* (measured within the meridian plane) and R_2 is the conjugate radius which is measured as the distance from *p* to axis *x* along he normal to the oocyte at point *p*. For most of the successful piercing experiments, presented in [21], the location *s* where the total curvature $K=0$ is claimed to be very close to 0.8. This signature ($K = 0$ at $s = 0.8$) is taken to be the identifier of desirable starting point for Ros-Drill© action. However due to the high-computational demand of this method (about 1.89 s computation time per frame), it cannot be executed in real time, and therefore it is not as effective as the radial deformation method that is pursued in this section. The intent of this comparison is to show the close correlation between the two approaches.

To establish the comparison platform, a closer look at the curvature variations is taken in the cases which were conducted during the present study (Figure 3.2) especially at the points of Ros-Drill© initiations. When the correspondence vis-à-vis in the tests presented is tabulated, the similarities are observed (Figure 3.3).

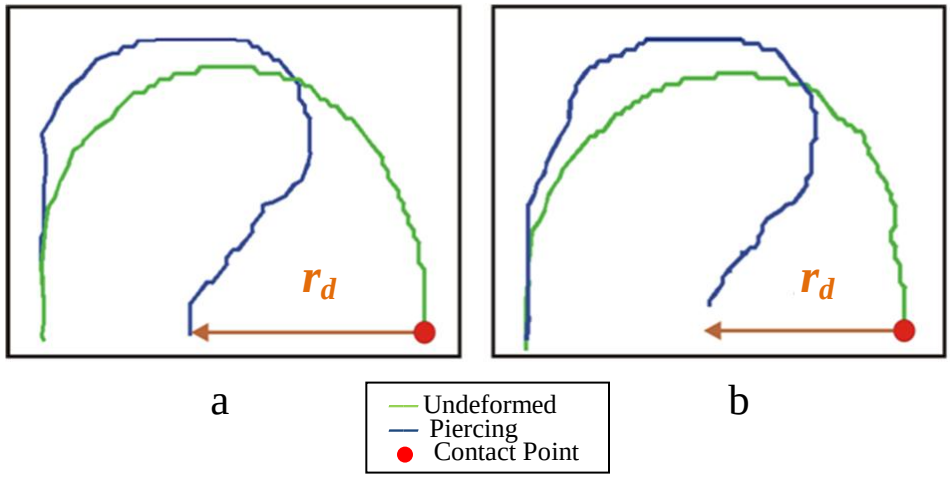

FIGURE 3.2: Two stages in radial deformation of cell membrane. a. Piercing at 60% and b. Piercing at 55%

FIGURE 3.3: a. Radial deformation and b. Values of *s* for *K*=0 when piercing

For the first case in which the desired amount of radial deformation is set to 60% of d_0, the piercing occurs when $K=0$ at s = 0.836. For the second case, where the amount of deformation is 55%, the piercing occurs for K= 0 at s = 0.873. The additional cases of 65% d_0 deformation (which are not reported in Figure 3.2) produced $K=0$ at around s = 0.8. These results strengthen the observations that the radial deformation based determination of automated Ros-

Drill© initiations would be in strong agreement with the curvature based strategy. The latter being a computationally costly process, therefore, the former is selected for the future ICSI tests.

The results shown in this study validate the action of Ros-Drill© for the empirically measured range of amounts of deformation. The drilling action starts when the desired distance d_d is reached. This outcome is not definitive; many other tests in which the specialist varies in a wider range the radial deformation r_d are yet to be done. With this as target, the optimal radial deformation that reaches the highest efficiency when piercing and facilitates the future stages in the oocyte development can be found.

3.2 EXPERIMENTAL AND SIMULATION RESULTS OF ROTATIONAL AUTOMATION

The controller (section 2.2) is first designed off-line in SIMULINK for frequencies ranging from 400 to 700 Hz [25]. By simulation, the adaptive look-up table in which control gains for a particular frequency can be found (Table 1). This look-up table is implemented in the C8051F120, achieving satisfactory tracking performance of the sinusoid. This adaptive tuning method is validated by comparing the experimental and SIMULINK results. In this experiment, a secondary DSP card of DSpace1104 is also utilized to process the encoder signal from the precision micro motor. This seamless connection enables the capture of the encoder signal with ease in the "control desk" platform. In Figure 3.4 and 3.5, SIMULINK and experimental results are shown for some operating frequencies.

They match each other by displaying the same desired peak to peak measurements of four steps.

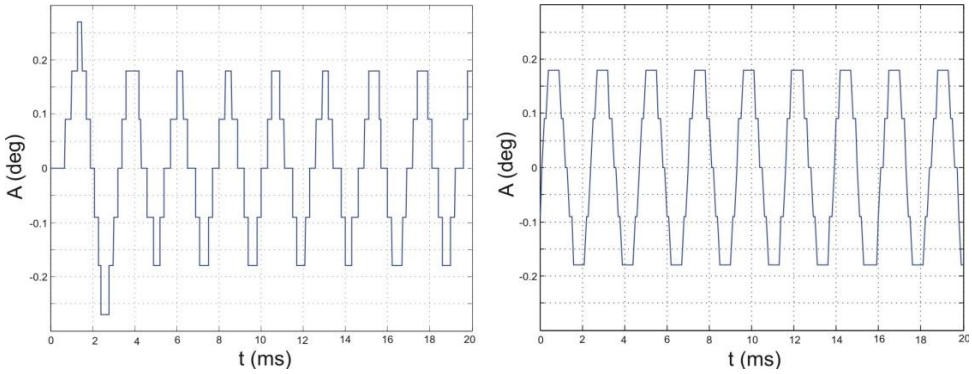

FIGURE 3.4: a. Simulation and b. Experimental results for f_a= 400 Hz

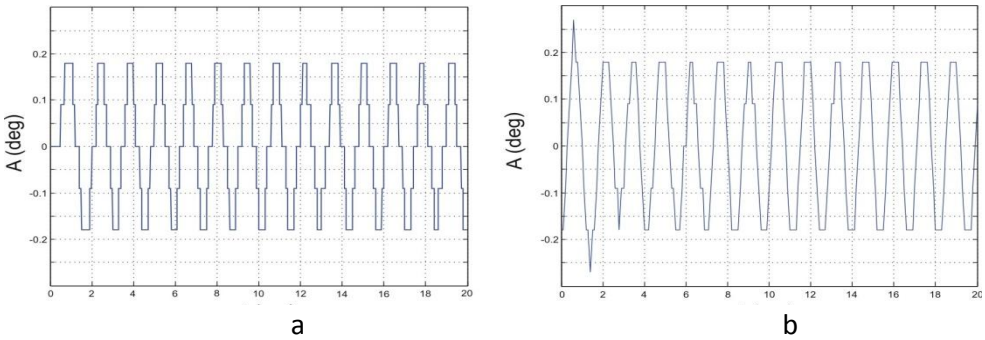

FIGURE 3.5: a. Simulation and b. Experimental results for f_a= 714 Hz

However, not always pure and constant-amplitude feedback profiles can be obtained. The discretization effect of the encoder over the real motion in the motor prevents the controller from having an exact match for the desired trajectory. It is also found that the initial position of the shaft, which is related to the position of the encoder board, affects the quality of the feedback signal. An analysis on this issue is presented in next section.

3.3 ANALYSIS OF NEW TRACKING PROFILES

Upgrading Ros-Drill© prototype to a higher level of performance (hardware and software) while keeping the principle of oscillatory rotational motion in ICSI trials, delivers a much deeper and meaningful advancement not only for the control of this application but for a more general field where precise motion is required and feedback mechanisms are not capable to create them due to sensory limitations.

In this section, a comparison between the α prototype tracking outcomes and the new results is presented, as well as an analysis of amplitude precision and reliability for the β prototype tracking results.

- COMPARISON BETWEEN ROS-DRILL© VERSIONS

Recalling what was proposed in previous works [11-12], Ros-Drill© α prototype consisted of a controller unit plus a servo-motor with a digital encoder. This structure is the same one utilized although the components may vary as seen next.

In the α prototype a PLC (programmable logic controller) was utilized as the control unit. The PLC, a robust controller offers reliable but somehow limited capabilities for applications that demand precision and speed. ICSI trials have pushed further the use of higher frequencies that ideally must offer better performance when drilling cell membranes. Because of this, the range of desired frequencies is increased (400-700 Hz instead of 100-500Hz) in the present work. In the other hand, the amplitude measurement induces a critical aspect in the

control strategy. If the sensing mechanism if not precise enough, there will not be sufficient information to establish a proper comparison between the desired trajectory (θ_d - θ_a) and the actual one θ_{enc}. This coarse error calculation can lead to barely acceptable profiles; therefore the lower the amplitude of the oscillatory profiles the worse the tracking is. The minimum possible amplitude to be measured with the α prototype is 0.176 deg. If the desired amplitude A_d is 0.2 degrees as established for better biological results, the tracking trajectory would have only one step of amplitude. The problem here is that this representation (0.176 deg of amplitude) would be valid for any desired amplitude no bigger than two times the resolution, that is, 0.352 degrees. For instance in Figure 3.6 a common profile for low amplitude and high frequency created by the first version of Ros-Drill© is shown. Here the desired trajectory is defined as a wave of A_d = 0.3 degrees and f_d = 500Hz (blue line).

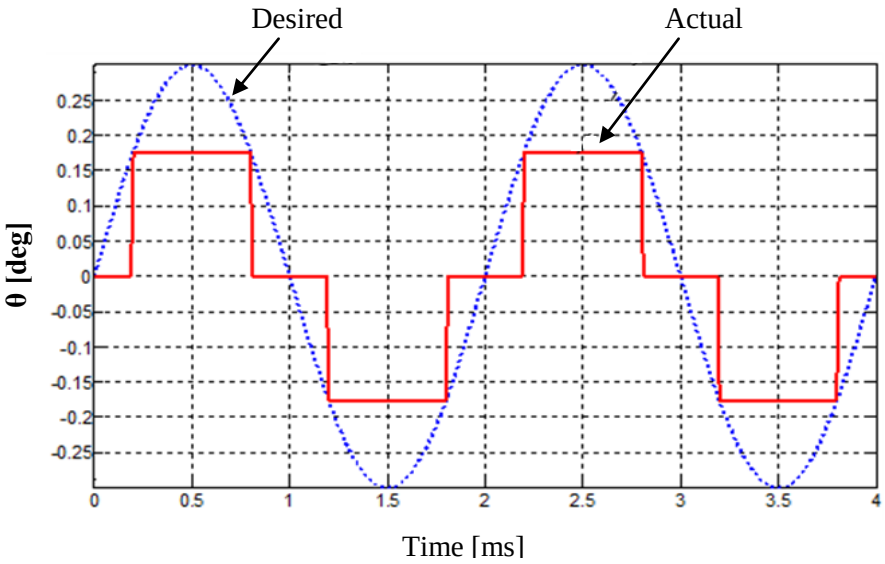

FIGURE 3.6: α version of Ros-Drill© , desired and tracking profiles

It can be seen that the encoder reading (feedback measurement – red line) still delivers a signal of only one step of amplitude. This fact leads to a very coarse tracking with an error of 58% in amplitude.

In the previous section, the modifications in hardware and software were explained in detail. The new microcontroller battles the shortfall given by the low sampling speed of the PLC (1000 Hz), reaching a comfortable level of work with f_s = 10000 Hz. In Table 2 a summary of the main differences between the two versions is presented.

Ros-Drill©	**Sampling**	**Encoder lines**	**Encoder resolution**
First	1000 Hz	512	0.176 (deg)
New	10 000 Hz	1000	0.09 (deg)

TABLE 2: Main differences between α and β versions of Ros-Drill©

In Figure 3.7 it can be observed the improved tractability for a desired trajectory with A_d = 0.2 degrees and f_d = 500 Hz. The increased resolution (smaller step – 0.09) doubles the number steps for the feedback making a more accurate recording of the actual motion. This results in a better error calculation and consequently in a better controlled motion by using an adaptive control technique [25].

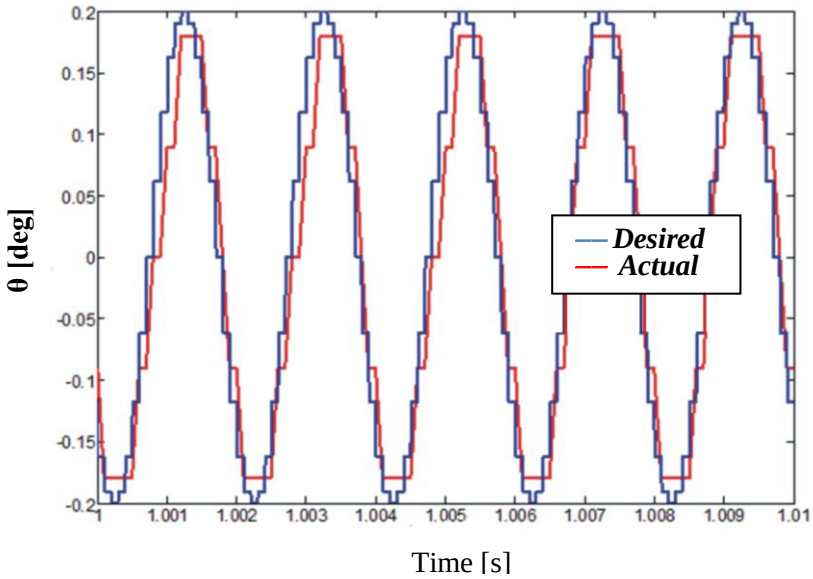

FIGURE 3.7: β version of Ros-Drill© , desired and tracking profiles

Due to this improved tractability, from this point on all the coming ICSI trials will be executed using the enhanced Ros-Drill©. Therefore it is decided to deepen in the analysis of the encoder reading. This trajectory reflects the real motion transmitted to the tip of the injecting pipette, and its similarity with the desired trajectory represents how good it is. It is important to notice that there will be always a difference between both trajectories depending on the initial position of the shaft when the oscillations are to be started. This gives the final contribution of this work. In spite that the desired trajectory is artificially created within the microcontroller and output to the motor, before this study there was no certainty about the reliability of the control signal that activated the rotational oscillations. With the next analysis a good estimate can be extracted based on the feedback signal.

- AMPLITUDE TRACKING ANALYSIS

In Figure 3.8 the sensing ability of the encoder is depicted on a hypothetical oscillation motion θ, the green dashed line. A_1 and A_2 are the upper and lower amplitude of θ respectively and let $A_{12}=A_1+A_2$. The red solid line is the discretized sensing of the encoder reading (θ_{enc}). Δ is used to represent the resolution of the encoder and a is defined as the encoder offset angle, the angle between the LED and its left nearest border in the encoding board before the encoder begins to rotate (shaft initial position). The offset a is uniformly distributed in $0 < a < \Delta$. The encoder can only be triggered when θ reaches $-a+\Delta$, $-a+2\Delta$, …, $-a+n\Delta$ in clockwise direction and $-a$, $-a-\Delta$, …, $-a-n\Delta$ in the counterclockwise direction, as indicated in Figure 3.8. The encoder may sense the same θ differently, depending on its offset angle, a.

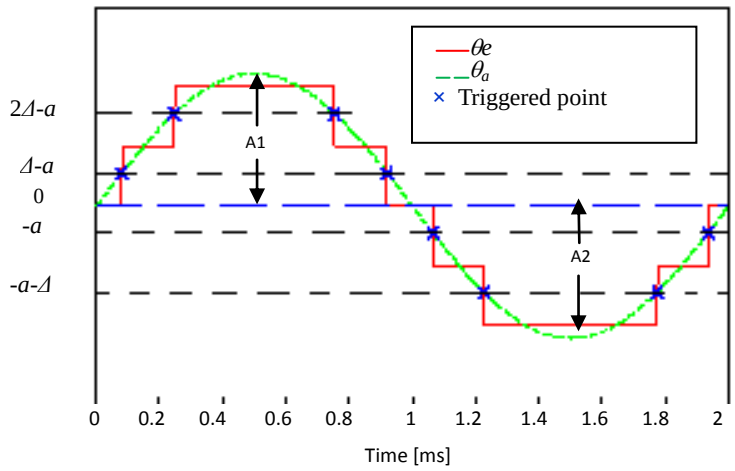

FIGURE 3.8: Oscillation motion θ read by the encoder (red discrete lines represent the encoder signal); $0<a<\Delta$ is the random offset angle).

The offset a hugely influences the quality of the feedback signal (encoder reading). Depending on the initial position of the shaft at the moment when the control signal is sent out to the microcontroller, the feedback signal can present some differences in its peak to peak measurements under same working settings (e.g., parameter settings). To prove this possibility, two sample cases are presented. In both of them, the desired trajectory is created with fluctuating amplitude A_d to check the encoder signal, and realize how much the response gets affected.

The resolution of the current encoder is Δ=0.09 deg. In the first case the desired peak-to-peak amplitude changes between 3Δ and 4Δ (Figure 3.9 – blue line). This variable-amplitude control signal will hit at different positions the encoder board, making it sense a variable amplitude feedback signal too (Figure 3.9 – red line). If this happens in practice, it can deliver some insights about the performance of the control. It cannot be said that the control is bad at all, counting on the fact that the feedback mechanism precision is poor (low resolution). What it does say, is that the digital representation of the encoder signal covers a range of amplitudes for the control signal. In other words, it can be expected a variation in the output even if the desired trajectory generation is clean. All of this because the big step of the encoder (009 deg) in comparison with the intended amplitude (0.2 deg) allows a huge gap for the initiating offset a. In the case presented here, offset a=0.764 deg, close to 0.09 deg. This offset makes the encoder shoot very fast the digital measurement because only a small real displacement of 0.0136 degrees is required to reach the next division line in the encoder.

In the second case (Figure 3.10) the peak-to-peak amplitude varies from 2Δ and 5Δ. A bigger change in the input creates a bigger change in the encoder reading. In this case the feedback signal can hit up to 5 steps of resolution.

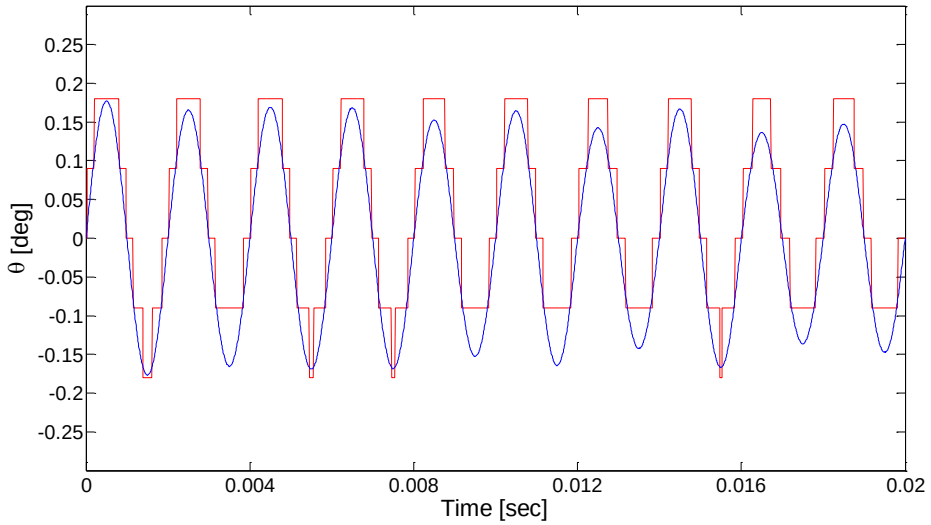

FIGURE 3.9: $3\Delta < A_{12} < 4\Delta$, a=0.0764

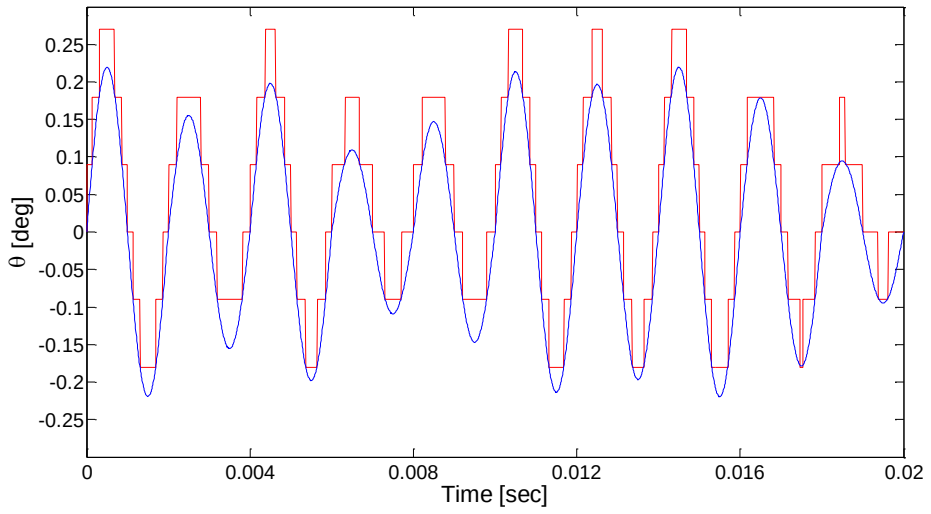

FIGURE 3.10: $2\Delta < A_{12} < 5\Delta$, a=0.0874

In this example, offset a=0.0874 degrees causes a similar encoder reaction to that presented for the previous example. The encoder will follow almost instantaneously the desired trajectory because only a very small displacement of 0.026 deg must be tracked to reach the first encoder line. If the offset value a was to be smaller the digital measurement of the feedback signal (red representations in Figure 3.9 and 3.10) would be a little bit phase shifted with respect to the desired trajectory θ , since the difference Δ-a would be greater and more time would be involved to reach the first encoder line.

With this analysis the probability of catching certain number of pulses under the desired trajectory effect can be foreseen. Therefore, the input can be further manipulated (in terms of amplitude) to obtain a better feedback profile.

3.4 BIOLOGICAL RESULTS OF β ROS-DRILL© IMPLEMENTATION

A new round of biological experiments was conducted at the University of California, Davis by a biologist in May 2011. In these experiments, β Ros-Drill© was programmed to operate in the same two modes used with the initial α prototype [10-11]:

1) high rotational amplitude at low frequency to separate sperm heads from tails, and

2) low rotational amplitude at high frequency to pierce and penetrate the oolemma. Visual feedback control was not used during these tests.

A biologist was trained on β Ros-Drill© within hours. This prototype offers a user- friendly interface and all of its parameters can be controlled by

simply adjusting some multi-position switches. They facilitate the proper selection of the desired trajectories as shown in previous sections (Fig. 2.27). The preparation of the biological material (sperm and oocytes) remained the same as in [11] in order to compare the performances. The differences presented in this new experiment arose mainly in the technical implementation of β Ros-Drill©. The experimental plan was as follows:

1. Testing of piercing modes and oscillatory motion using different set of parameters (rotational amplitudes, frequencies and the duration) with no injection of sperm head. Survival of the oocytes after penetration is recorded for each selection to determine the most convenient set of (amplitude, frequency and duration) combinations.
2. Testing of sperm head separation (again using some specially selected amplitude, frequency and durations (as explained in [11]).
3. Complete ICSI test to determine the embryo development after the Ros-Drill based ICSI.

For point (1) it was found that the drilling protocol used with α Ros-Drill© (A_d=0.3 deg and f_d=500Hz) could not offer any surviving oocytes with β version, even though in the newest version the duration of the oscillations is precisely controlled. Many factors might be involved in this considerable difference as shown later.

The operating frequency is increased (up to 700 Hz) and the amplitude is reduced further (down to 0.1 degree). These selections were made due to the

noticeably high lateral oscillations on the oocytes (and even at the holding pipette) when the Ros-Drill© action took place. These occurrences never reported in the earlier version (alpha) Ros-Drill©. In that regard, **this round of tests was unsuccessful** to perform the planned Ros-Drill© piercing operations. These trials resulted in the following set of parameters which gave promising survival levels after piercing. They are shown in Table 3.

In this test, five batches of oocytes were utilized. Piercing was successful in all the attempts, however, the number of trials (3 to 9) is undesirably high and different for each group. It is important to emphasize that even oocytes from the same group (e.g., same mother, equal time of collection) may present differences in their properties, making the parameter-selection process a hard task.

Amplitude [deg]	Frequency [Hz]	Duration [sec]	# oocytes	#trials (average)	Pierced	Survival	Survival Rate (%)
0.1	700	0.48	9	3	9/9	2/9	22.2
0.1	700	0.48	8	5	8/8	7/8	87.5
0.1	700	0.48	9	5	9/9	3/9	33.3
0.1	700	0.48	11	6	11/11	8/11	72.7
0.1	700	0.48	12	4	12/12	8/12	66.6

TABLE 3: Survival rate after piercing (no sperm injection) using β Ros-Drill©

As shown in Table 3, having A_d=0.1 deg and f_d=700Hz with a duration of 0.48 seconds the oocytes respond positively to the penetration of the pipette. This set is chosen as the new protocol for the complete ICSI tests.

Test set (2) refers to the sperm head separation task. This task works on the same principle, rotational oscillations at a certain frequency during an exact time. The difference consists in the value of these parameters. We started using the

protocol recommended for this mode with α Ros-Drill© (A_d=3 deg and f_d=50Hz) [11] but a tuning was required for β Ros-Drill©. We started increasing the amplitude but no separation occurred. We considered it a failure if more than 5 trials were needed to break the sperm head from the tail.

Amplitude [deg]	**Frequency [Hz]**	**Duration [sec]**	**# oocytes**	**#trials (average)**
3	50	0.125	3	15
5	50	0.125	3	12
8	50	0.125	3	10
3	100	0.125	20	2

TABLE 4: Sperm head separation tests using β Ros-Drill©

In Table 4 we can observe the sequence followed until a proper parameter set was determined. The biologist showed his comfort in breaking sperm heads with Ros-Drill©.

To finish up these set of tests we performed a complete ICSI experiment (3). Here, the biologist worked with six batches of oocytes as listed in Table 5. For each group he did sperm head separation right before the injection. The protocols for each mode are as described before: Sperm head separation (A_d=3 deg, f_d=100Hz and duration of 0.125 sec) and drilling (A_d=0.1 deg, f_d=700Hz and duration of 0.48 sec).

	Amplitude [deg]	Frequency [Hz]	Duration [sec]	# oocytes	#trials (average)	Pierced	Survival	Survival Rate (%)
SP1	3	100	0.125	9	2	NA	NA	NA
D1	0.1	700	0.48	9	12	9/9	5/9	55.5
SP2	3	100	0.125	9	1	NA	NA	NA
D2	0.1	700	0.48	9	9	9/9	3/9	33.33
SP3	3	100	0.125	10	1	NA	NA	NA
D3	0.1	700	0.48	10	5	10/10	0/10	0
SP4	3	100	0.125	9	2	NA	NA	NA
D4	0.1	700	0.48	9	6	9/9	1/9	11.1
SP5	3	100	0.125	14	1	NA	NA	NA
D5	0.1	700	0.48	14	6	14/14	4/14	28.5
SP6	3	100	0.125	10	2	NA	NA	NA
D6	0.1	700	0.48	10	9	10/10	1/10	10
	TOTAL DRILLING			61	8	61/61	14/61	23
				1 HOUR LATER			8/61	13.11

TABLE 5: ICSI tests using β Ros-Drill©

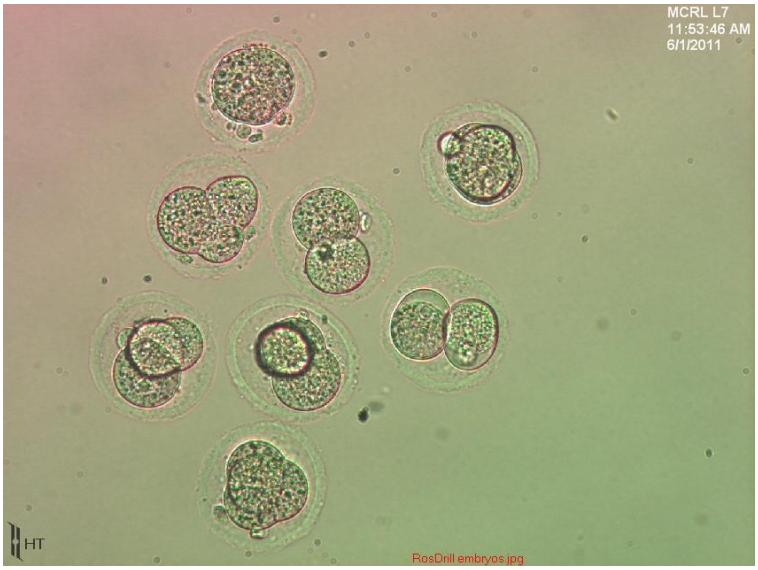

FIGURE 3.11: Development of survived oocytes

One hour after the experiment we had only 8 alive oocytes out of 61. The oocytes were cultured and placed in the incubator to follow up their development.

After 96 hours they were checked and only two developed to morula. The remaining six stopped their growing process at 2 or 3-4 cell stages (Fig. 3.11).

Finally we decided to make a mechanistic test (without an oocyte). We increased the frequency up to 1000 Hz by modifying the code in the controller. This option was not available to the user. When testing Ros-Drill© at this frequency we observed an undesired behavior. The pipette was shaking more visibly and some noise could be heard. In order to analyze this performance we executed the same experiment in our laboratory in Connecticut, where we could capture the desired trajectory. A lot of noise appeared in this profile altering the oscillations. The power spectrum (Fig. 3.12) shows clearly the frequency components of the signal.

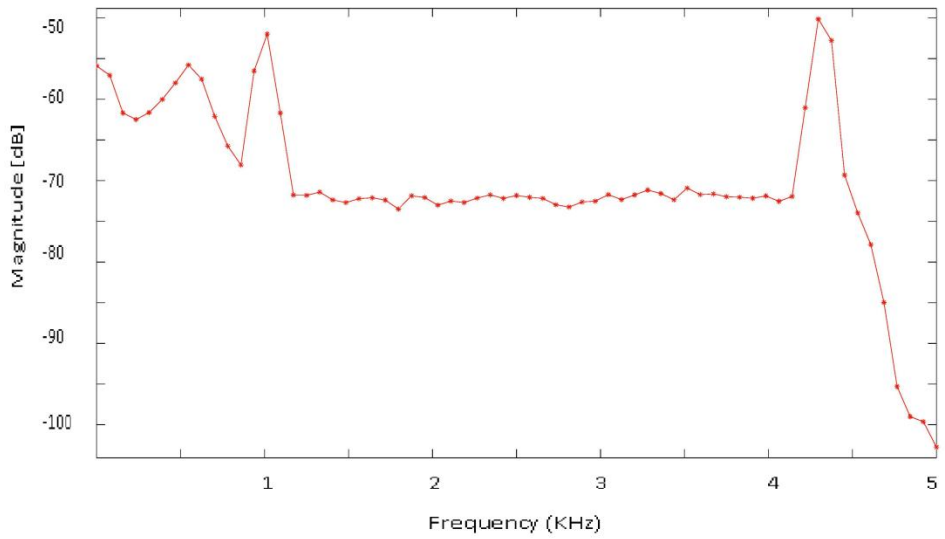

FIGURE 3.12 Power Spectrum of profile (A_d=0.1 deg, f_d=1000Hz)

There are two outstanding peaks in the plot. One is located at 1000 Hz and the other around 4.5 KHz. The first one corresponds to the desired trajectory and

by default this should be the only one with high amplitude, however, the second peak at higher frequency corresponds to the noise present in the oscillations. As seen in the figure, both peaks have comparable magnitudes allowing a rough calculation of the SNR (signal to noise ration) equal to 1. In terms of quality this is not good, since the desired trajectory is not dominant in the behavior of the oscillations; nevertheless it is an interesting case because we are tracking visibly a very small amplitude control signal. This opens up the possibility of re-tuning the controller for an open-loop control strategy at higher frequencies if such small amplitude is to be used. Many more experiments must be executed to take Ros-Drill© to a state of smooth performance. In these tests we observed a trend of reducing amplitude and increasing frequency that worked out.

4. CONCLUSIONS AND FUTURE WORK

In this thesis a novel microinjection technology for ICSI, which is called Ros-Drill©, is further studied from the perspective of automated initiation of rotations and feedback control tracking of oscillatory motion of the pipette tip. The starting instant of the rotational drill operation is correlated to the variation of the membrane curvature of the oocyte. The curvature measurements are made using computer vision. Based on repeated experiments and corresponding geometric observations we can state that the most effective piercing takes place when the membrane displays a certain radial deformation. It is quantifiable and therefore it forms a practical control criterion towards an automated deployment of Ros-Drill© operations. This new development also has potential applications in the areas of cryopreservation and therapeutic cloning.

Visual feedback based automatic initiation of Ros-Drill© action is presented for mouse oocyte piercing prior to ICSI. A real-time algorithm is developed to track the tip of the injection pipette. The trials demonstrate that the real-time execution of the algorithm is possible. User interface that are necessary for this process is minimized to a couple of manual selections in a fixed frame in the "off-line" phase of the work. The efficiency of the method is experimentally validated, and has successfully compared with the earlier curvature based effort. Validation of a heuristically measured range for amount of deformations and curvatures is also presented.

Ros-Drill© device is greatly improved (from α to β version). Modifications in hardware as well as in software were successfully implemented. To mitigate

the restriction imposed in the previous design a new microcontroller with better features is utilized along with a higher resolution encoder, however, restrictions still exist mainly due to the coarse resolution of the sensor. Utilizing a new PID tuning method [25] these problems are coped. The hybrid system with position sensor with low-resolution is accurately modeled in SIMULINK so that the PID gains sets for any frequency tuned in this SIMULINK model are used in the experiment. SIMULINK and experimental results match each other by displaying the same desired peak-to-peak measurements.

Regarding the biological results of the implementation of the β version, conducted in MBP laboratory in Davis we observed that it delivered a considerably lower survival and development rates compared with the α-Ros-Drill© tests [11]. This is disappointing especially considering the introduction of a powerful microcontroller to the β-Ros-Drill© set up.

Conducting a careful analysis after the tests, we notice unacceptably high level of lateral oscillations at the oocyte during the Ros-Drill© action. Making numerous experimental verifications, we conclude that the biggest cause of the failure was the eccentricity in the transmission linking the motor shaft to the pipette tip (Fig. 1.2). Bearings, coupling, and the motor shaft were misaligned forcing the tip shake (sometimes violently). To complement the powerful micro-controller we foresee the need for a much better alignment tools to be utilized. This may require a redesign of some of the relevant components (coupling, connecting material etc.). The remedial measure to reduce the oscillation amplitudes from 0.3 or 0.2 degrees to 0.1 was not necessarily ideal, because this

modification pushes the extreme limits of the controller. Notice that the resolution of the present encoder is 0.09 degrees and the desired amplitude is 0.1 degrees. This means that the encoder is working on the edge of its capabilities presenting two problems: 1. the controller has less points to execute the adaptive PID control strategy. This leads to a very coarse error signal and 2. The encoder may skip some readings due to the limited control signal, making the error signal even worse. This implies that at these conditions the controller behaves more like an open loop adaptive controller.

Many other factors might have also affected the outcome of the experiments. They are mostly of empiric nature and especially the biological properties of the tested subjects may vary. For instance, a critical step in piercing is the slight aspiration of the membrane just prior to the Ros-Drill© action. The biologist sucks the membrane inside the pipette prior to the start of drilling. This obviously is quite empirical and changes from oocyte to oocyte. That is why the average of number of trials changed significantly between the different batches.

APPENDIX I
GENERAL SCHEME β ROS-DRILL©

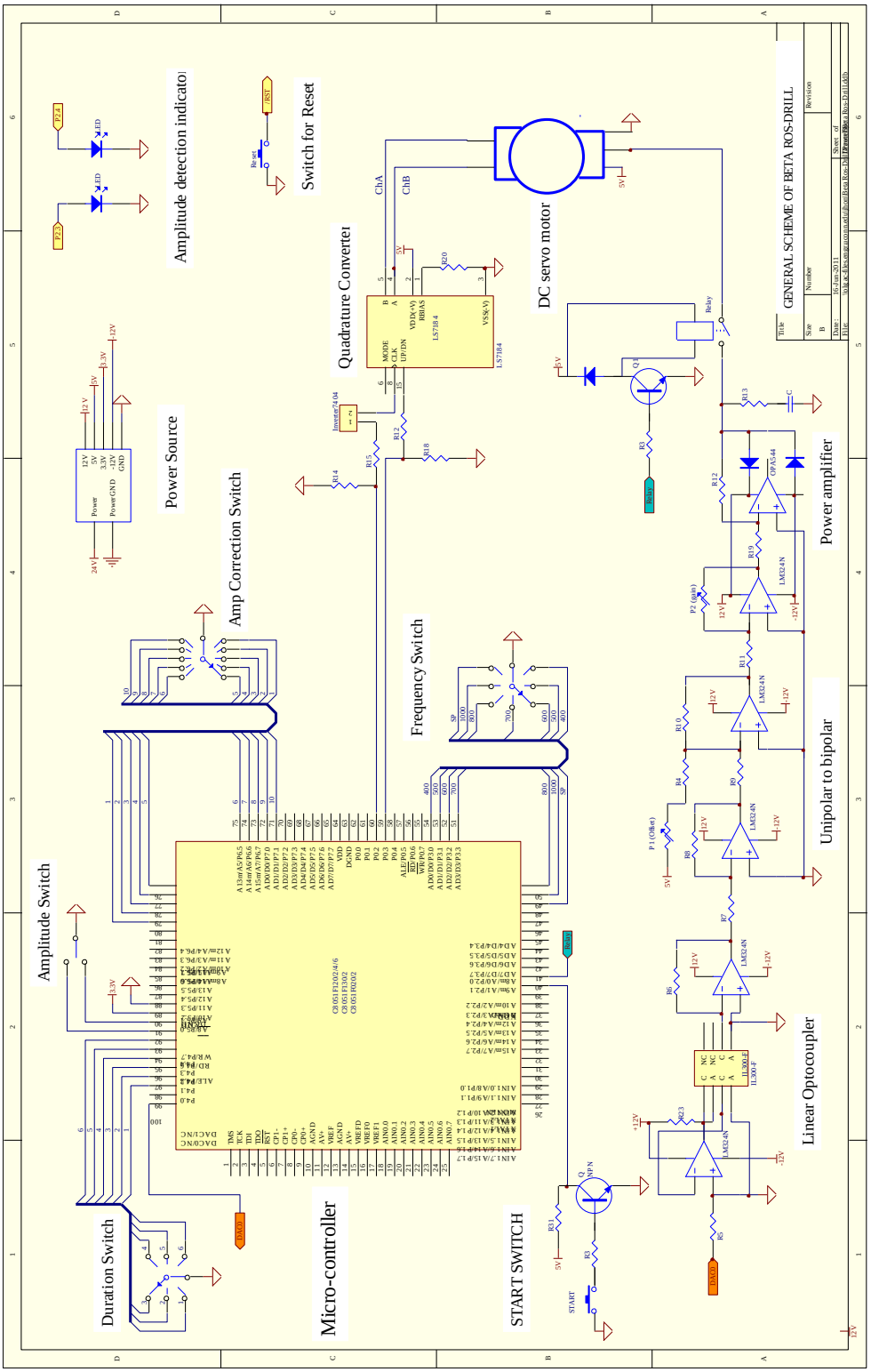

DETAILED SCHEMES OF DRIVER CARD FOR β ROS-DRILL©

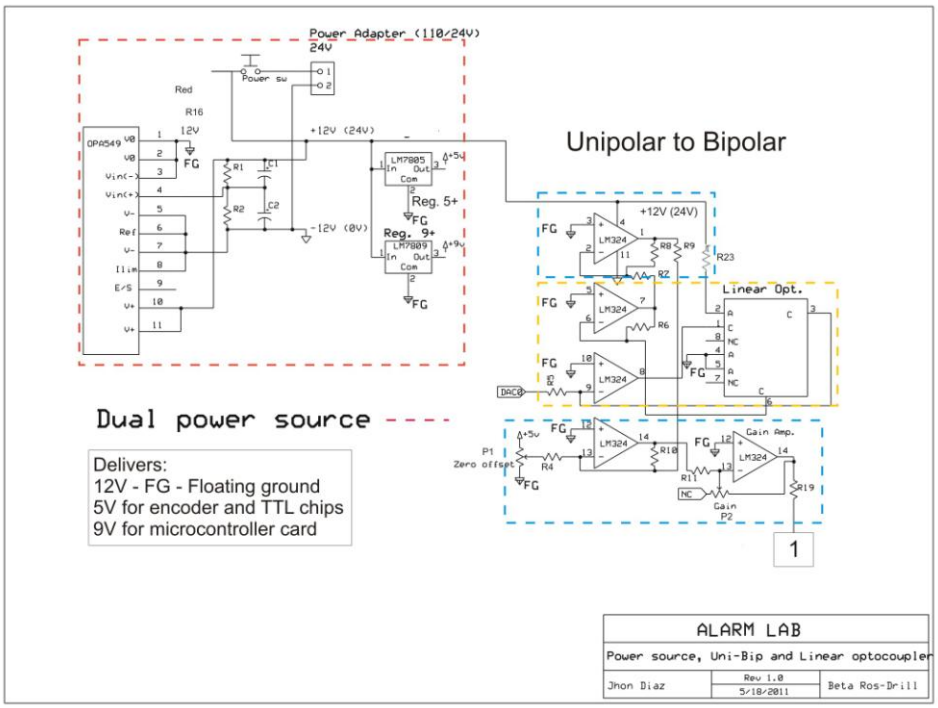

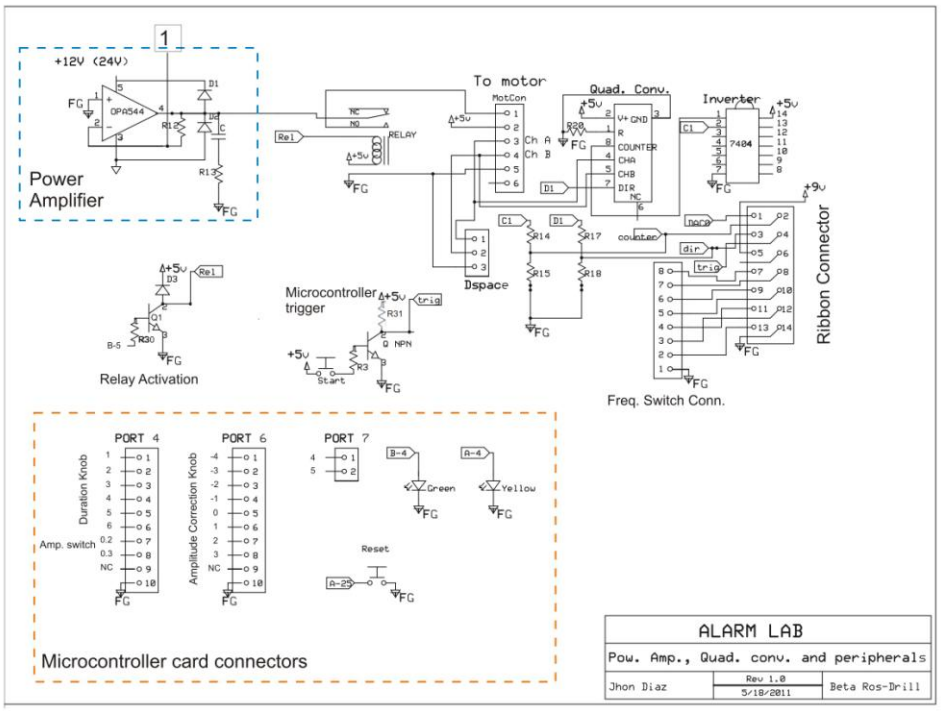

LIST OF CONNECTIONS

Driver Card Connectors

Ribbon Connector

Pin #	I/O	Description	Micro. pin	Microcard	Wire color	
1	I	DAC0	DAC0	C-26	yellow	
2	O	Counter	P0.2	A-12	pink	*Quad. Conv. -
3	O	Direction	P0.3	C-11	red	Encoder
4	O	Start	P2.7	A-5	brown	
5	O	9V			black	*Power of microcontroller card
6	NC				white	This has a small 2-pin connector
7	O	400Hz	P3.0	A-10	gray	
8	O	500Hz	P3.1	C-9	purple	
9	O	600Hz	P3.2	B-9	blue	
10	O	700Hz	P3.3	A-9	green	
11	O	800Hz	P3.4	C-8	yellow	
12	O	1000Hz	P3.5	B-8	pink	
13	O	SP-100Hz	P3.6	A-8	red	
14	GND	GND			brown	

*This is the connector between the driver card and the microcontroller card

* SP stands for Sperm separation mode, D for drilling mde

Frequency switch connector

Pin #	I/O	Description	RS pin	Wire color
1	GND	GND	pole	brown
2	I	SP-100Hz	8	red
3	I	1000Hz	7	pink
4	I	800Hz	6	yellow
5	I	700Hz	5	green
6	I	600Hz	4	blue
7	I	500Hz	3	purple
8	I	400Hz	2	gray

*This is the connector between the driver card and the rotary switch for frequency selection

*RS - Rotary switch

To motor connector

Pin #	I/O	Description	Motor	Wire color
1	O	V+	1	yellow
2	O	5V	2	blue
3	I	ChA	3	red&white
4	I	ChB	4	red&white
5	GND	GND	5	Orange

Cable to motor β-PT1	
Wire color	**Description**
Black	V+
Orange	5V
Green	ChA
White	ChB
Blue	GND

Cable to motor β-PT2	
Wire color	**Description**
Brown	V+
White	5V
Red	ChA
Green	ChB
Blue	GND

Microcontroller card connectors

Port 4					
Pin #	**I/O**	**Description**	**Wire color PT1**	**Wire color PT2**	
4.1	I	Duration 1	yellow	brown	
4.2	I	Duration 2	pink	red	
4.3	I	Duration 3	red	pink	
4.4	I	Duration 4	brown	yellow	
4.5	I	Duration 5	black	green	
4.6	I	Duration 6	white	blue	
4.7	I	Amp 1	purple	purple	*This switch controls
4.8	I	Amp 2	green	gray	amplitude of both modes:
4.9	NC				D and SP
4.10.	GND	GND	brown + blue	black + white	

Port 6 and Port 7			
Pin #	**I/O**	**Description**	**Wire color**
6.1	I	Kd adj. -4	red
6.2	I	Kd adj. -3	pink
6.3	I	Kd adj. -2	yellow
6.4	I	Kd adj. -1	green
6.5	I	Kd adj. 0	blue

6.6	I	Kd adj. 1	purple
6.7	I	Kd adj. 2	gray
6.8	I	Kd adj. 3	white
6.9	NC		
6.10.	GND	GND	pink
7.1	I	Kd adj. 4	black
7.2	I	Kd adj. 5	brown

LIST OF COMPONENTS

Beta Ros-Drill©		
Components	**Description**	**Quantity**
microcontroller card	PCB C8051120	1
R1, R2	1K	1
R3,R30,R31	2.2K	1
R14,R17,R23	1K	1
R15,R18	2K	1
R5,R6	39K	1
R7,R8,R10,R4	33K	1
R9,R11,R12,R19	15K	1
R22	33K	1
R13,R16	290	1
R20	2M	1
OPA549	Power amp. power source	1
Heatsink	For opa549	1
Switch (power)	on/off	1
2-pin connector		4
LM7805	5V regulator	1
LM7809	9V regulator	1
LM324	OpAmps	2
14-pin dip socket	For IC	3
Linear Optocoupler	IL-300	1
P1	Pot. 10K	1
P2	Pot. 500K	1
C1,C2	220 uF	1
C	0.1 uF	2
Diode D1, D2, D3	1N41007	1
OPA544	Power amp. to motor	1
Relay JS 5V	Relay to motor	1
Swtich (NO) - start	Foot pedal	1
jack phone connector	for foot pedal	1

Connector 6 pins	male and female -To motor	1
Connector 8 pins	male and female - Freq. switch connector	1
Connector 3 pins	male and female	1
Ribbon connector 14 pins	male	1
Transistor Q	npn	2
Quadrator converter	LS7814	1
Inverter	7404	1
10-pin dip sockets	for IC	2
10-pin 2 row female connector	for IC	2
rotary switch 10 pos	frequency selection and Amplitude correction	2
rotary switch 6 pos	Duration	1
switch 2 pos	Amplitude	1
Power adapter	24 V, 3 A	1
Enclosure	OKW B3015227	1
Front panel	OKW B3115267	1
5-pin din female connector	Front panel motor connection	
5-pin din male connector	Front panel motor connection	
Swtich (NO) - reset	Front panel reset button	1
LED (yellow, green, red)	Indicators	1
motor	Brushed motor 2342, 1000 lines encoder	1

DRIVER CARD PCB

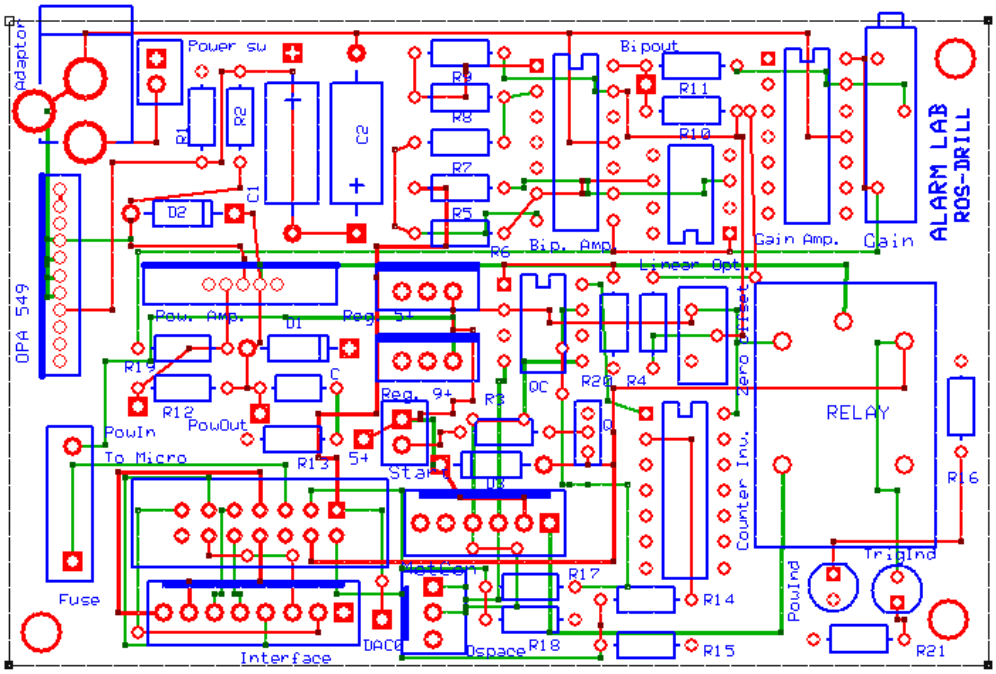

REFERENCES

[1] Collas, P., and Barnes, F.L. 1994. Nuclear transplantation by microinjection of inner cell mass and granulose cell nuclei. *Mol. Reprod. Dev*. 38 (3), 264-267.

[2] Meng, L., and Wolf, D.P. 1997. Sperm-induced oocyte activation in the rhesus monkey: Nuclear and cytoplasmic changes following intra-cytoplasmic sperm injection. *Hum Reprod* 1062-1068.

[3] Takeuchi, S., Minoura, H., Shibahara, T., Shen, S., Futamura, N., and Toyoda, N. 2001. Comparison of piezo assisted micromanipulation with conventional micromanipulation for intra-cytoplasmic sperm injection into human oocytes. *Gyn. Obs. Inv*. 52 (3), 158-162.

[4] Yanagimachi, R., 2005. Intracytoplasmic injection of spermatozoa and spermatogenic cells: its biology and applications in humans and animals. *Reprod Biomed Online* 10, 2

[5] Li, M.W. and Lloyd, K. C. K., 2006. Intracytoplasmic sperm injection in the mouse. In "Principles and Practice: Mammalian and Avian Transgenesis – New Approaches". (Eds S. Pease and C. Lois) pp. 23-40. (Springer–Verlag, Berlin, Heidelberg.)

[6] Kimura Y., and Yanagimachi R. 1995. Intracytoplasmic sperm injection in the mouse. *Biol Reprod* 52, 709-720.

[7] Huang, T., Kimura, Y., and Yanagimachi, R. 1996. The use of piezo micromanipulation for intracytoplasmic sperm injection of human oocytes. *J Assist Reprod Gen.* 13(4), 320-328.

[8] Kawase, Y., Iwata, T., Ueda, O., Kamada, N., Tachibe, T., Aoki, Y., Jishage, K.-I., and Suzuki, H. 2002. Effect of partial incision of the zona pellucida by piezo-micromanipulator for in vitro fertilization using frozen-thawed mouse spermatozoa on the developmental rate of embryos transferred at the 2-cell stage. *Biol Reprod* 66, 381-385.

[9] Ediz, K., and Olgac, N. 2004. Micro-dynamics of the piezo-driven pipettes in ICSI. *Biomed. Eng. IEEE Trans Biomed Eng* 51(7), 1262-1268.

[10] Ediz, K., and Olgac, N., 2005. Effect of mercury column on the microdynamics of the piezo-driven pipettes. *J. Biomech. Eng.* 127, 531-535.

[11] Ergenc, A.F., Li, M.-W., Toner, M., Biggers, J.D., Kent Lloyd, K.C. and Olgac, N. 2008. Rotationally Ocillating Drill (Ros-Drill©) for mouse ICSI without using mercury. *Mol. Reprod. Dev.* 75(12) 1744-1751.

[12] Ergenc, A.F., and Olgac, N., 2007. New technology for cellular piercing: rotationally oscillating micro-injector, description and validation tests. *Biomed. Microdevices* Vol. 9, no. 6, 885-891.

[13] Gonzalez, R, 2008. *Digital Image Processing, Third Edition. Pp. 149.*

[14] Pozrikidis, C., 1997. *Introduction to Theoretical and Computational Fluid Dynamics*, Oxford University Press, New York.

[15] Press, W.H., Teukolsky, S.A., Vetterling, W.T., Flannery, B.P., 1988. *Numerical Recipes in C: The Art of Scientific Computing*, Cambridge University Press, New York.

[16] Hayter, A.J., 1995. *Probability and Statistics for Engineers and Scientists*, PWS Publishing Company, Boston.

[17] Sun, Y., and Nelson, B.J. 2002. Biological cell injection using an autonomous microrobotic system. *Int J Robot Res* Vol. 21 (10-11), 861-868.

[18] Mattos, L., Grant, E., and Thresher, R. 2006. Speeding up video processing for blastocyst microinjection. *IEEE International Conference on Intelligent Robots and Systems*. 5825-5830.

[19] Mattos, L., Grant, E., Thresher, R., and Kluckman K. 2008. From teleoperated to automatic blastocyst microinjections: designing a new system from expert-controlled operations. *IEEE/RSJ International Conference on Intelligent Robots and Systems.* 4036-4041.

[20] Pillarisetti, A., Anjum, W., Desai, J.P., Friedman, G., and Brooks, A.D. 2005. Force feedback interface for cell injection. *Proceedings of the First Joint Eurohaptics Conference and Symposium on Haptic Interfaces for Virtual Environment and Teleoperator Systems.*

[21] Diaz, J., Karzar-Jeddi, M., Olgac, N., Fan, T., and Ergenc, A. 2009. On the geometric characteristics of cell membrane using rotationally oscillating drill Ros-Drill©. Proceedings of the ASME Dynamic Systems and Control Conference DSCC2009.

[22] Hu, G.-S., Digital Signal Processing, 2nd ed. Beijing: Tsinghua Univ. Press, 2005

[23] Ogata, K., System Dynamics, 3rd ed. Prentice Hall, 1998 Renkens, M.J.M., 1997. Design of an Axially Controlled Spindle Unit for High Precision Diamond Turning, Ph.D. Thesis, Eindhoven University of Technology, The Netherlands, ISBN 90-74445-35-7.

[24] Astrom, K.J., PID Controllers: Theory, Design, and Tuning, 2nd ed. ISA, 200

[25] Zhang, Z., Diaz, J. and Olgac, N. Adaptive Hybrid Control for Rotationally Oscillating Drill (Ros-Drill©) with Low-Resolution Feedback. 2011